Manuscript + supp figures

Click here to access/download;Manuscript;PLoS_pred_coding_2.pdf

Predictive Coding Models for Pain Perception

Yuru Song[1,2,†], Mingchen Yao[1,3,†], Helen Kemprecos[4], Áine Byrne[5], Zhengdong Xiao[1], Qiaosheng Zhang[6], Amrita Singh[6], Jing Wang[6,7,8], Zhe S. Chen[1,7,8*]

1 Department of Psychiatry, New York University School of Medicine, New York, New York, United States of America

2 Department of Biology, University of California, San Diego, California, United States of America

3 Kuang Yaming Honors School, Nanjing University, Nanjing, Jiangsu, China

4 Department of Biochemistry, New York University, New York, New York, United States of America

5 Center for Neural Science, New York University, New York, New York, United States of America

6 Department of Anesthesiology, Pain and Operative Medicine, New York University School of Medicine, New York, New York, United States of America

7 Department of Neuroscience and Physiology, New York University School of Medicine, New York, New York, United States of America

8 Neuroscience Institute, New York University School of Medicine, New York, New York, United States of America

† These authors contributed equally. * Corresponding email: zhe.chen@nyulangone.org

ORCID 0000-0002-6483-6056 (Z. S. Chen)

ORCID 0000-0002-2794-0014 (M. Yao)

ORCID 0000-0002-8424-8710 (A. Byrne)

ORCID 0000-0003-0485-3126 (Q. Zhang)

ORCID 0000-0003-1580-1356 (J. Wang)

Abstract

Pain is a complex, multidimensional experience that involves dynamic interactions between sensory-discriminative and affective-emotional processes. Pain experiences have a high degree of variability depending on their context and prior anticipation. Viewing pain perception as a perceptual inference problem, we use a predictive coding paradigm to characterize both evoked and spontaneous pain. We record the local field potentials (LFPs) from the primary somatosensory cortex (S1) and the anterior cingulate cortex (ACC) of freely behaving rats—two regions known to encode the sensory-discriminative and affective-emotional aspects of pain, respectively. We further propose a framework of predictive coding to investigate the temporal coordination of oscillatory activity between the S1 and ACC. Specifically, we develop a high-level, empirical and phenomenological model to describe the macroscopic dynamics of bottom-up and top-down activity. Supported by recent experimental data, we also develop a mechanistic mean-field model to describe the mesoscopic population neuronal dynamics in the S1 and ACC populations, in both naive and chronic pain-treated animals. Our proposed predictive coding models not only replicate important experimental findings, but also provide new mechanistic insight into the uncertainty of expectation, placebo or nocebo effect, and chronic pain.

Author Summary

Pain perception in the mammalian brain is encoded through multiple brain circuits. The experience of pain is often associated with brain rhythms or neuronal oscillations at different frequencies. Understanding the temporal coordination of neural oscillatory activity from different brain regions is important for dissecting pain circuit mechanisms and revealing differences between distinct pain conditions. Predictive coding is a general computational framework to understand perceptual inference by integrating bottom-up sensory information and top-down expectation. Supported by experimental data, we propose a predictive coding framework for pain perception, and develop empirical and biologically-constrained computational models to characterize oscillatory dynamics of neuronal populations from two cortical circuits—one for the sensory-discriminative

experience and the other for affective-emotional experience, and further characterize their temporal coordination under various pain conditions. Our computational study of biologically-constrained neuronal population model reveals important mechanistic insight on pain perception, placebo analgesia, and chronic pain.

Introduction

Pain is a basic experience that is subjective and multidimensional. Pain processing involves sensory, affective, and cognitive processing across distributed neural circuits [1–5]. However, a complete understanding of pain perception and cortical pain processing has remained elusive. Given the same nociceptive stimuli, the context matters for pain percept. Human neuroimaging studies have shown that among many brain regions, the primary somatosensory cortex (S1) and the anterior cingulate cortex (ACC) are the two most important areas involved in pain processing. The S1 represents the sensory-discriminative component of pain, whereas the ACC represents the affective-motivational component of pain [2, 6]. In addition, ACC neuronal activities have been shown to correlate with noxious stimulus intensities, and chronic pain can alter acute pain intensity representation in the ACC to increase the aversive response to noxious stimuli at anatomically unrelated sites [7]. In addition to the bottom-up input, top-down attention, expectation, or contextual factors can bias cortical pain processing or modulate the strength or salience of pain signals [8]. Descending modulation can attenuate the incoming nociceptive signal and further skew the subjective pain perception despite the high-intensity noxious stimulus input.

Evoked pain is triggered by noxious sensory stimuli, whereas spontaneous (or tonic) pain is not. Spontaneous pain can be induced by repeated noxious stimulations in naive animals, or induced by chronic pain conditions [9]. Pain perception has been conceptualized as perceptual inference [8], and predictive coding may provide a theoretical model for characterizing such inference [10, 11]. Specifically, pain perception can be studied as an inferential process in which prior information is used to generate expectations about future perception and to interpret sensory input.

Predictive coding paradigms describe the inversion of a generative model of the percept and constantly adapt the hypothesis of sensory perception [12]. A predictive

model characterizes the uncertainty of sensory inputs in time and space [13]. Predictive coding relies on correcting errors resulting from comparisons between internal predictions and actual observations. Such paradigms have provided important insights into perceptual inference, sensory processing, motor control, and multi sensory integration [14–17]. Predictive coding has been suggested as a universal computational principle in the neocortex [18, 19], and this framework may accommodate various data modalities and across multiple spatiotemporal scales [20].

The experience of pain is often associated with brain rhythms or neuronal oscillations at different frequencies [11, 21]. For multisite recordings, it is important to investigate the inter-regional local field potential (LFP) oscillatory coordination [22], as interareal oscillatory synchronization plays an important role in top-down neocortical processing [23]. In a series of rodent pain experiments, we collected various *in vivo* neurophysiological data (spikes and LFP) from single or two brain regions in freely behaving rats [7, 24–26]. These data have established the foundation towards improved understanding of pain perception as well as empirical evidence for computational modeling.

Here we present a predictive coding framework to model the temporal coordination of interareal oscillatory activity between the rat S1 and ACC during evoked and spontaneous pain episodes. We first develop a *macroscopic* empirical model to characterize the temporally coordinated Z-scored LFP power from these brain regions and then replicate our empirical experimental findings. We further develop a biologically-constrained *mesoscopic* mean field model to characterize the S1 and ACC population neuronal activity in various pain conditions, for both naive and chronic pain-treated animals. To our best knowledge, our modeling effort is the first systematic investigation towards understanding pain perception within the predictive coding framework. Overall, predictions from our predictive coding models provide new mechanistic insights into the uncertainty of expectation, placebo or nocebo effect, and chronic pain.

Materials and Methods

Experimental protocol and recordings

All experimental studies were performed in accordance with the National Institutes of Health (NIH) *Guide for the Care and Use of Laboratory Animals* to ensure minimal animal use and discomfort, and were approved by the New York University School of Medicine (NYUSOM) Institutional Animal Care and Use Committee (IACUC).

Male adult Sprague-Dale rats (250-300 g, Taconic Farms, Albany, NY) were used in our current study and kept at the new Science Building at NYUSOM, with controlled humidity, temperature and 12-h (6:30 a.m.-6:30 p.m.) light-dark cycle. Food and water were available ad libitum. Animals were given on average 10 days to adjust to the new environment before the initiation of experiments.

Thermal pain stimuli were used for freely exploring rats in a plastic chamber of size $38 \times 20 \times 25$ cm^3 on top of a mesh table. A blue (473 nm diode-pumped solid-state) laser with varying laser intensities was delivered to the rat's hindpaw. The laser stimulation was delivered in repeated trials (25-40) during 30-45 min. Two video cameras (120 frame per second) were used to continuously monitor the rat's behavior during the course of experiment. Details are referred to previous publications [7, 25].

To produce chronic inflammatory pain, 0.075 ml of *Complete Freund's adjuvant* (CFA) (mycobacterium tuberculosis, Sigma-Aldrich) was suspended in an oil-saline (1:1) emulsion, and injected subcutaneously into the plantar aspect of the hindpaw opposite to the paw that was stimulated by a laser; namely, only a unilateral inflammation was induced. In CFA rats, laser stimulations were delivered to the opposite paw of the injured foot. The ACC and S1 electrodes were implanted on the contralateral side of the stimulated foot (Fig. 1A) .

Repeated noxious laser stimulations to the rat hindpaw could induce spontaneous pain behaviors. During the inter-trial intervals, we examined the rat's behavior to identify putative spontaneous pain episodes (such as twitch, lifting/flicking, paw withdrawal and paw licking). Due to the lack of ground truth, we referred to those events as spontaneous pain-like episodes [26].

We used silicon probes (Buzsaki32, NeuroNexus) with 3D printed drive to record

multi-channel (up to 64 channels) neural activities from the rat ACC and S1 areas simultaneously, on the contralateral side of the paw that received noxious stimulation. For surgery, rats were anesthetized with isoflurane (1.5%-2%). The skull was exposed and a 3 mm-diameter hole was drilled above the target region. The coordinates for the ACC and S1 implants were: ACC: AP 2.7, ML 1.4-2.0, DV 2.0, with an angle of 20° toward the middle line; S1: AP −1.5, ML 2.5-3.2, DV 1.5. The drive as secured to the skull screws with dental cement. We used a Plexon (Dallas, TX) data acquisition system to record *in vivo* extracellular neural signals at a sampling rate of 40 kHz. The signals were first band-pass filtered (0.3 Hz-7.5 kHz), and LFPs were obtained upon subsequent band-pass filtering (1-100 Hz).

Data analysis

Time-frequency analyses. Based on the simultaneously recorded multichannel LFP signals from the S1 and ACC, we applied the principal component analysis (PCA) and extracted the dominant principal component (PC) for the S1 and ACC, respectively. We then computed the spectrogram of the PC for each region. Multitapered spectral analyses for LFP spectrogram were performed using the Chronux toolbox (chronux.org). Specifically, we chose a half-bandwidth parameter W such that the windowing functions were maximally concentrated within $[-W, W]$. We chose $W > 1/T$ (where T denotes the duration) such that the Slepian taper functions were well concentrated in frequency and had bias reducing characteristics. In terms of Chronux function setup, we used the tapers setup $[TW, N]$, where TW is the time-bandwidth product, and $N = 2 \times TW - 1$ is the number of tapers. Since the taper functions are mutually orthogonal, they give independent spectral estimates. In all time-frequency analyses, we used a moving window length of 500 ms and a step size of 1 ms. We used $TW = 5$. From the spectrogram, we computed the Z-scored spectrogram, where the baseline was defined as the 5-s period before the stimulus presentation.

Pain-responsive neurons. To identify pain-responsive neurons, we used a previously established criterion [25]. Specifically, we computed the Z-scored firing rate related to the baseline (3-5 s before the stimulus onset). A neuron was called a positive pain-responding neuron if the following two criteria were satisfied: (i) the absolute value

of the Z-scored firing rate of least one time bin after stimulation must be greater than 2.5, and (ii) if the first criterion is met, at least the next two bins must be greater than 1.65. These criteria must be fulfilled within 3 s after the stimulus onset.

Unless stated otherwise, all statistical tests were nonparametric tests without the normality assumption.

A framework of predictive coding for pain

Predictive coding is aimed at minimizing the prediction error (PE) and further using it to update the new prediction. The schematic diagram of predictive coding is shown in Fig. 2. In what follows, we propose the stochastic differential equations (SDEs) to describe the neural oscillatory dynamics in both bottom-up and top-down pathways.

To explain the predictive coding idea, we first introduce some basic notations. Specifically, let the latent variable z denote the subjective pain percept, let x denote the observed stimulus input, and let u and v represent the proxy for the observed gamma activity from the S1 and the beta activity from the ACC, respectively.

Bottom-up and top-down pathways. In the bottom-up pathway, we assume that dynamics of u are driven by the prediction error (PE) between the stimulus input and expectation, as follows

$$\xi(t) = |x(t) - z(t)| \tag{1}$$

$$\tau_u \frac{\mathrm{d}u(t)}{\mathrm{d}t} = -u(t) + \Pi_1 \xi(t) + \epsilon_u \tag{2}$$

where $\tau_u > 0$ denotes the time constant or step size to reach a steady state; ϵ_u denotes the additive Gaussian noise. The variable ξ denotes the PE: the difference between the bottom-up finite-duration sensory input x and top-down pain-induced expectation z (Fig. 2A); Π_1 is a gain parameter known as step size, which weights the PE to serve as a driving force in Eq (2).

The gain parameter Π_1 can be interpreted as a precision (i.e., inverse of variance) parameter (Fig. 2B). The inverse of variance is also known as the "surprise" signal. To see this link, we can assume that there is an expectation uncertainty of $z(t)$, or equivalently, the PE $\xi(t) = |x(t) - z(t)|$. If $x(t)$ is deterministic, then the variance of PE

is computed as $\mathrm{Var}[\xi(t)] = \mathrm{Var}[z(t)] = 1/\Pi_1$. Therefore, the precision parameter controls the step size of the dynamics update in Eq (2). If the uncertainty of the expectation is large, the step size will be small (or the update will be conservative); if the uncertainty is low, the update will be more aggressive.

The S1 is known to project to the ACC [27, 28]. In the S1→ACC pathway, in the simplest form, we assume that the dynamics of v are driven by the signal consisting of a time-delayed $u(t - \Delta_u)$ (where $\Delta_u > 0$) and the pain percept, as follows

$$\tau_v \frac{\mathrm{d}v(t)}{\mathrm{d}t} = -v(t) + \Pi_2 u(t - \Delta_u) + \Pi_3 z(t) + \epsilon_v \tag{3}$$

where $\tau_v > 0$ denotes the time constant, and ϵ_v denotes the additive Gaussian noise. Similarly, Π_2 is a gain parameter that scales the PE to obtain a new prediction (Fig. 2C), and Π_3/Π_2 defines the relative gain between the two inputs $z(t)$ and $u(t - \Delta_u)$. The coupling dependency between u, v and x is shown in Fig. 2D.

In the top-down pathway, the predictive coding uses the PE to update the expectation after a certain delay. Specifically, we assume that the dynamics of pain percept z follow a linear differential equation as follows

$$\tau_z(t) \frac{\mathrm{d}z(t)}{\mathrm{d}t} = -z(t) + x(t - \Delta_x) + \epsilon_z \tag{4}$$

$$z(t) = 0 \quad \text{if} \quad \int_{t'}^{t} z(\tau)\mathrm{d}\tau > Z_{\text{threshold}} \tag{5}$$

$$\tau_z(t) = \frac{a}{1 + b\exp(x(t))} \tag{6}$$

where ϵ_z denotes the additive Gaussian noise. In Eq (5), $z(t)$ is reset to 0 after an accumulative preset threshold $Z_{\text{threshold}}$ within a moving window is reached to trigger an escape-type pain behavior (e.g, paw withdrawal). Equation (6) imposes an inverse sigmoid-shaped relationship between the input amplitude $x(t)$ and time constant τ_z. The initial pain percept $z(0)$ is either zero (no-anticipation), negative value (placebo), or positive value (nocebo or pain anticipation).

For convenience, we refer to the macroscopic predictive model model described by Eqs (1)-(6) as the *empirical model*. The variables u and v can be interpreted as the Z-scored LFP gamma and beta power (see Discussion). The choice of time delay Δ_u reflected the event-related potential (ERP) latency between the S1 and ACC; their time

constants τ_u and τ_v were also chosen accordingly. Based on different assumptions of x and z, we simulated the dynamics of u and v from Eqs (1)–(3).

Computing time-averaged power. From the simulated traces of $u(t)$ and $v(t)$, we computed the averaged power before and after the withdrawal. Specifically, let $A_u = \frac{1}{t_r}\int_0^{t_r} u(t)\mathrm{d}t$ denote the averaged area from the start of computer simulation to the reset (withdrawal) time t_r, and let $A_v = \frac{1}{T-t_r}\int_{t_r}^{T} v(t)\mathrm{d}t$ denote the averaged area lasting the same duration it took to reach the $Z_{\text{threshold}}$ from the reset (withdrawal) time. Therefore, A_u and A_v could be viewed as the averaged pre- and post-withdrawal Z-scored power, respectively.

Fourier analysis. Taking the Fourier transform of Eq (3) and rearranging the terms, we obtained the mapping of u and v in the frequency domain:

$$V(\omega) = H_1(\omega)U(\omega) + H_2(\omega)Z(\omega) + H_3(\omega)W_v(\omega) \tag{7}$$

where $H_3(\omega)$ (or $H_2(\omega)$) is a transfer function between $V(\omega)$ and $W_v(\omega)$—spectrum for white noise (or $Z(\omega)$, unobserved); and $H_1(\omega)$ is a transfer function between $V(\omega)$ and $U(\omega)$:

$$H_1(\omega) = \frac{\Pi_2}{(j\omega\tau_v + 1)e^{j\omega\Delta_u}} \approx \frac{\Pi_2/2}{(j\omega\tau_v + 1)[(j\omega\Delta_u + 1)^2 + 0.5]}$$

where $j = \sqrt{-1}$, and the approximation is derived from the 2nd-order Taylor series expansion: $e^s \approx 1 + s + \frac{1}{2}s^2 = \frac{1}{2}[(s+1)^2 + 0.5]$. The first term of the denominator in $H_1(\omega)$ is a 1st-order low-pass filter, and the second term is a 2nd-order low-pass filter; together, $H_1(\omega)$ operates as a low-pass filter that attenuates the high-frequency (e.g., gamma-band) activity $U(\omega)$, resulting in a lower-frequency (e.g., alpha or beta-band) activity $V(\omega)$ in the top-down pathway (Fig. 2E). This also explains the reason why the Z-scored power is shifted from the S1 gamma-band (bottom-up) to the ACC beta-band (top-down).

Mean field models

To better describe the population neuronal dynamics, we introduce a mechanistic model, with explicit excitatory and inhibitory populations and synapses, to the predictive coding framework described above. To achieve a trade-off between biological complexity and modeling complexity, we opt for a mean field model [29,30].

Background. The main assumption of mean field models is that tracking the average activity, e.g., mean firing rate and mean synaptic activity, is sufficient when modeling populations of neurons. Given the extensive number of neurons and synapses in even a small area of cortex, this is a reasonable assumption. One of the first mean field models of neural activity is attributed to Wilson and Cowan [30]. This two-dimensional model tracks the mean firing rate of an excitatory population of neurons coupled to an inhibitory population of neurons, and has been successfully used to describe visual hallucinations [31,32], binocular rivalry [33], epilepsy [34,35], resting brain state activity [36], traveling cortical waves [33,37], and cortical resonant frequencies [38].

We propose a Wilson-Cowan (WC)-like model, with the addition of a synaptic variable for each of the neuronal population. For a single brain area, this amounts to four differential equations [39]:

$$\tau_{r_E}\frac{\mathrm{d}r_E}{\mathrm{d}t} = -r_E + f(w_{EE}s_E - w_{IE}s_I + P_E), \tag{8}$$

$$\tau_{r_I}\frac{\mathrm{d}r_I}{\mathrm{d}t} = -r_I + f(w_{EI}s_E - w_{II}s_I + P_I), \tag{9}$$

$$\tau_{s_E}\frac{\mathrm{d}s_E}{\mathrm{d}t} = -s_E + \gamma_E r_E(1 - s_E), \tag{10}$$

$$\tau_{s_I}\frac{\mathrm{d}s_I}{\mathrm{d}t} = -s_I + \gamma_I r_I(1 - s_I), \tag{11}$$

where $r_{E/I}$ is the population firing rate of the excitatory/inhibitory population, and $s_{E/I}$ is the synaptic activation of the corresponding population. Each variable has a corresponding time constant τ. The inter- and intra-populations coupling strengths are set by $\{w_{EE}, w_{IE}, w_{EI}, w_{II}\}$; $P_{E/I}$ represents the external input from elsewhere in the cortex; and $\gamma_{E/I}$ is the ratio between activation and inactivation times of the synapse.

As in the standard Wilson-Cowan model, f is a sigmoid function,

$$f(x) = \frac{1}{1 + \mathrm{e}^{-\sigma(x-h)}}, \tag{12}$$

where σ is the slope and h is the threshold.

In this study, we are interested in the interaction of the S1 and ACC, and consider a model with two excitatory-inhibitory (E-I) pairs, as described by Eqs (8)–(11) (Fig. 3A). Our recent experimental findings have provided strong evidence that that there is a direct S1→ACC projection, which plays an important role in pain processing [22, 27, 28]. In contrast, less is known about the role of the ACC→S1 pathway in cortical pain processing. For the sake of simplicity, we have neglected feedback in our initial model.

Biologically-constrained mean field model. We have recently combined optogenetics and electrophysiology to dissect the ACC circuit in pain processing (A. Singh, unpublished data). We have found a direct S1→ACC projection engaged in cortical pain processing. Notably, in naive rats, only a small percentage of the ACC population was pain responsive (10-15%). Among those pain responsive neurons, about 20% of the population received a direct input from the S1 (Fig. 1E). Of the ACC neurons which receive input from S1, 37% of them were pain responsive. However in CFA rats, those two percentages increased to 32% and 52%, respectively (Fig. 1F).

Based on these findings, we made two modifications to the computational model. First, the S1→ACC pathway is modeled with the inclusion of an additional term in Eq (8) for the ACC population; namely, we changed the input P_E^{ACC} to $P_E^{\mathrm{ACC}} + s_E^{\mathrm{S1}}(t - \Delta_{\mathrm{S1}})$, where the excitatory input from the S1 is delayed by a positive Δ_{S1}.

Second, we divided the excitatory ACC neuronal population into two subpopulations $E_{2\text{-}1}$ and $E_{2\text{-}2}$ (Fig. 3B), one of which directly receives S1 input ($E_{2\text{-}1}$), while the other is indirectly driven by the former one ($E_{2\text{-}2}$). Therefore, we revised the model with two excitatory-inhibitory (E-I) groups, as described by Eq (8)–(11).

We also scaled the inter- and intra-populations coupling strength by the relative population sizes. For example, if the S1 population is twice as large as the ACC population, then the coupling strength of S1→S1 and S1→ACC would be twice as large

as those of ACC→S1 and ACC→ACC, respectively. Here we have assumed that there are 20% of ACC excitatory neurons that receive S1 inputs; κ is the S1/ACC neuronal population size ratio; ρ scales the inhibitory/excitatory strength; L is the scaling of long-range projection between the two regions. We set w_{EE} and w_{EI} as the basic coupling strength, and set other coupling strength with a proper scaling constant (Fig. 3B).

Furthermore, we assumed that the external inputs were applied equally to the excitatory and inhibitory populations of the S1 and ACC as follows

$$\begin{aligned} P_E^{\mathrm{S1}}(t) = P_I^{\mathrm{S1}}(t) &= g^{\mathrm{S1}}|x(t) - z(t)|, \\ P_E^{\mathrm{ACC}}(t) = P_I^{\mathrm{ACC}}(t) &= g^{\mathrm{ACC}} q_i z(t - \Delta_x). \end{aligned}$$

where g^{S1} and g^{ACC} denote the two gain parameters for respective neuronal population, and Δ_x denotes the time delay from the input x. Let $\mathrm{S1}^+$ (or $\mathrm{S1}^-$) denote the ACC population that receives direct S1 input (or not); let q_i with subscript index $i = \mathrm{S1}^+, \mathrm{S1}^-, I$ denote the percentages of pain-responsive neurons in subpopulations $E_{2\text{-}1}$, $E_{2\text{-}2}$ and I_2, respectively.

Computing the power using the envelope function. We computed the upper and lower envelopes of the oscillatory firing rate trace. We used the average (midline) of the upper and lower envelopes to calculate the time-averaged synaptic activation variable s (or alternatively, the firing rate variable r) as a measure of the firing dynamics in our mean field model.

To compute the pre-S1 synaptic activation, we integrated the average power of s_E^{S1} from baseline (by discarding the initial transient) to the withdrawal onset, and then normalized it by the duration. To compute the post-ACC synaptic activation, we integrated the average power of s_E^{ACC} from the withdrawal onset until a fixed window length, and then normalized it by the duration.

Software

The custom MATLAB code for implementing two computational models is distributed online (https://www.cn3lab.org/software.html).

Results

LFP oscillatory activity coordination in naive and chronic pain rats

From the recorded multichannel LFPs of the S1 and ACC, we computed the Z-scored spectrogram for pain episodes (time 0 represents the laser onset in evoked pain, and the withdrawal onset in spontaneous pain). During evoked pain, we usually observed event-related potentials (ERPs) in both S1 and ACC areas. Our prior report has indicated that the ERP latency was sooner (∼200-300 ms) in the S1 than in the ACC during evoked pain episodes [26]. In contrast, during spontaneous pain-like episodes, ERPs occurred in either the S1, or ACC, or both areas, with a high degree of variability in latency.

For spontaneous pain-like episodes, we investigated whether the LFP power in the ACC and S1 at the beta and/or gamma bands change in a spatiotemporally coordinated manner. We computed the 10-s LFP spectrograms centered around the spontaneous pain behavior onsets (pre-event: $[-5, 0]$ s, post-event: [0,5] s). To highlight the event-related synchronization/desynchronization (ERS/ERD) phenomenon, we computed the Z-scored pre-gamma power related to the post-event period, and computed the Z-scored post-beta power related to the pre-event period. We found that the averaged pre-event Z-scored gamma power in the S1 positively correlated with the averaged post-event Z-scored beta power in the ACC (Fig. 1C, left panel). This suggests that pre S1 gamma-ERS (or ERD) was temporally followed by post ACC beta-ERD (or ERS). Notably, the correlated ERS/ERD patterns became weaker during evoked pain episodes (Fig. 1C, middle panel) and disappeared in negative control (Fig. 1C, right panel). In chronic pain state, we also found similar observations in CFA rats (Fig. 1D).

In another independent investigation (A. Singh, unpublished data), we have established a direct S1→ACC projection during cortical pain processing. Among the pain-responsive ACC neuronal population, we have identified the subpopulation that received the direct S1 input, for both naive and CFA rats (Fig. 1E and Fig. 1F, respectively). Compared to naive rats, chronic pain increased the percentage of recorded ACC neurons that received the direct S1 input. Together, these findings provide

Table 1. Summary of default parameters used in the empirical model.

Parameter	Value
dt	1 ms
Time constant τ_u	200 ms
Time constant τ_v	300 ms
Time delay Δ_u	300 ms
Time delay Δ_x	300 ms
Gain parameter Π_1	1
Gain parameter Π_2	1
Gain parameter Π_3	1
Threshold $Z_{\text{threshold}}$	400
a in Eq (6)	4000
b in Eq (6)	1

empirical evidence to characterize chronic pain in our predictive coding model.

Computer simulations for the empirical model

The goal of the computational predictive coding model is to replicate the main findings of the pain experiments at the macroscopic level. From the SDEs, we ran numerical simulations to characterize the relationship of the surrogate of LFP oscillatory activity between the S1 and ACC. In the following computer simulations, we used the default parameters listed in Table 1. The additive Gaussian noise components $\{\epsilon_u, \epsilon_v, \epsilon_z\}$ were all assumed to have zero mean and unit variance. In each condition, we reported the mean statistics based on 30 independent Monte Carlo simulations.

Evoked pain. In the evoked pain condition, we set the initial pain expectation to be zero (i.e., $z(0) = 0$), and we set $u(0) = 0$ and $v(0) = 0$ for the initial Z-scored activity from the S1 and ACC. In addition, we set the pain stimulus $x(t) = 1$ if $t \in [4.5, 5]$ s and $x(t) = 0$ otherwise. Namely, the first 4-s period prior to the stimulus was treated as the baseline. Given the initial condition, we solved the first-order differential equations using the forward Euler method with time step 1 ms. An illustration of representative traces is shown in Fig. 4A. As seen in the figure, the z-trace closely followed the x-trace; the u trace reached an initial peak and gradually decays; and the v-trace decayed slower than the other traces.

The withdrawal latency following the noxious stimulus onset is a standard measure to quantify the acute pain behavior [40]. In our simulations, we used the duration between the onset of input $x(t)$ and the time of $z(t)$ reset as the proxy of withdrawal

latency. We found that the latency decreases with increased stimulus intensity or input amplitude (Fig. 4C). This is consistent with our prior experimental observations [41].

Spontaneous pain. In the spontaneous pain condition, we set $u(0) = 0, v(0) = 0, z(0) = 1$, $x(t) = 0$ (i.e., no stimulus), and $Z_{\text{threshold}} = 400$. An illustration of representative traces is shown in Fig. 4B. In this example, the z-trace decays exponentially until it reached the reset threshold (time axis 0); the u and v-traces first rose and then decayed exponentially, and it took a longer time for the v-trace to approach the baseline. From the u and v-traces, we computed the net area under the curve: the curve above 0 contributes to a positive area value, and the curve below 0 contributes to a negative area value.

To introduce trial variability, we assigned $z(0)$ with different values. By varying the initial condition $z(0)$, we obtained various mean statistics for A_u and A_v during spontaneous pain. The strong positive correlation between A_u and A_v (Fig. 4E) was found. In contrast, the correlation between A_u and A_v is weaker in the simulated evoked pain condition (Fig. 4B). These results are consistent with our experimental findings (Fig. 1B).

Placebo condition. Pain perception changes with different contexts. An identical noxious stimulus may cause distinct pain percept or behavior depending on the top-down influence. Placebo effects can create real or illusory pain analgesia, which can be pharmacological, psychological, or physical [42]. We assumed that the placebo analgesia biased the initial subjective pain percept $z(0)$. To simulate the placebo effect in the context of pain perception, we set $u(0) = 0, v(0) = 0, z(0) = -1$, and $x(t) = 1$ if $t \in [4.5, 5]$ s and $x(t) = 0$ otherwise. An illustration of representative traces is shown in Fig. 4F. As seen in the figure, because of the initial (negative) bias from z, the v-trace first dropped below 0 and then slowly rose; when the stimulus x appeared, the u and v-traces gradually rose until $z(t) = 0$ (reset point), and then decayed to baseline.

Furthermore, we varied $z(0)$ in the placebo condition and repeated 30 Monte Carlo simulations. A negative correlation between A_u and A_v was found (Fig. 4G).

Sensitivity analysis of gain parameters and transmission delay. Thus far, we have kept all gain (or precision) parameters in unity. Next, we investigated how the

change of gain parameter affects the dynamics. Since $\mathrm{Var}[z(0)] = 1/\Pi_1$, we further assumed that $\Pi_3 = \Pi_1$ in Eq (3). To investigate the impact of gain parameters, we considered two scenarios. In the first scenario, we set $\Pi_2 = 1$ and systematically varied Π_1 and Π_3 together. In the second scenario, we set $\Pi_1 = \Pi_3 = 1$ and systematically varied Π_2. In both scenarios, the ratio Π_3/Π_2 would deviate from unity. The results from these two scenarios are shown in Fig. 5. The qualitative phenomenon that describes the correlation between A_u and A_v were relatively robust with a wide range of gain parameters. In the evoked pain condition, the correlation value remained low. In the spontaneous pain condition, the correlation value showed an increasing trend with increasing Π_1 and Π_3, and showed a decreasing trend with increasing Π_2. In the placebo condition, the correlation value remained negative for most of the parameter setup.

In task behaviors, the cortico-cortical transmission delay may vary. For cortical communications over long-range connections or information relay between several brain areas, the transmission delay may be even longer. To investigate the impact of cortico-cortical transmission delay, we further varied Δ_u and examined the impact on the correlation statistic (Fig. 6). It was found that the correlation between A_u and A_v were relatively stable for a wide range of delay parameters.

In summary, these simulation results derived from the empirical model replicates several key findings for various pain experiments. However, the empirical model is rather abstract and the interpretation of the model parameter or results is thereby limited. Next, we extended the same line of investigations using the mean field model.

Computer simulations for the mean field model

In the following computer simulations, we used the default parameters listed in Table 2. We used the forward Euler method to numerically simulate the population dynamics for a total 5.5 seconds (time step 0.1 ms). The pulse input x had a 200-ms duration. A 2-s simulation interval was treated as the baseline period. The initial values of all $r_{E/I}$ and $s_{E/I}$ were set to zero. We computed the midline envelopes of the synaptic activation variable s and firing rate variable s of excitatory populations from the S1 and ACC. Notably, the synaptic activation variable s was also highly correlated with the firing rate variable r (Fig. S1), and here we used s to represent the firing dynamics of the S1

Table 2. Summary of standard mean field model parameters.

Parameter	Value
Firing rate of E/I population $r_{E/I}$	
Synaptic activation of E/I population $s_{E/I}$	
Time step in Euler's method	0.1 ms
Percentage of ACC population receiving a direct S1 input	20%
Excitatory synaptic weights $\{w_{EE}, w_{EI}\}$	22
Inhibitory synaptic weights $\{w_{II}, w_{IE}\}$	$w_{II} = \rho w_{EE}$
	$w_{IE} = \rho w_{EI}$
Scaling parameter ρ for inhibitory/excitatory strength	-1.5
Scaling parameter L for long-range projection	0.1
S1/ACC population size ratio κ	2
Gain parameter g^{S1}	2
Gain parameter g^{ACC}	5
Scaling parameter for % of pain-responsive neurons $q^{+}_{S1}, q^{-}_{S1}, q_I$	35%, 14%, 10%
Slope of sigmoid function $\sigma_E = \sigma_I$	S1: 0.5; ACC: 0.7
Center of sigmoid function $h_E = h_I$	S1: 4; ACC: 3
Synaptic activation time constant for excitatory population $\tau_{s,E}$	3 ms
Synaptic activation time constant for inhibitory population $\tau_{s,I}$	10 ms
S1 firing time constant for excitatory population $\tau_{r,E}$	1 ms
S1 firing time constant for inhibitory population $\tau_{r,I}$	3 ms
ACC firing time constant for excitatory population $\tau_{r,E}$	3 ms
ACC firing time constant for inhibitory population $\tau_{r,I}$	18 ms
Ratio between activation and inactivation times of the synapse $\gamma_{E/I}$	4
Time delay in S1→ACC projection: Δ_{S1}	20 ms
Time delay: Δ_x	20 ms

and ACC populations. Because the mean field model is aimed to characterize the mesoscopic neuronal population activity (as opposed to the macroscopic activity in the empirical model), it employs different time constants and delay parameters.

To simulate the withdrawal behavior, the reset time of latent variable z was determined when the integration of z from the stimulus onset (in the presence of stimulus) reached a predetermined threshold. When z was reset to 0, x was also simultaneously set to 0, indicating that the animal has withdrawn or escaped from the noxious stimulus. We ran numerical simulations for three pain perception conditions. With different x and z, we simulated the $r_{E/I}$ and $s_{E/I}$ dynamics of neuronal subpopulations in our mean field model.

Evoked pain. In the evoked pain condition, we set $a = 2000$ (Eq 6), $Z_{\mathrm{threshold}} = 300$, and $z(0) = 0$. The dynamics of the populations are shown in Fig. 7A. In our simulation, all populations have an oscillatory activity with stable frequency, where the S1 population oscillates in the gamma-band frequency and the ACC population in the

beta-band frequency. For each population, we took the upper and lower envelope of oscillation and computed their averaged power as a representation of the mean synaptic activation (Fig. 7B). As seen in the figure, S1 firing increased quickly after the stimulus onset, as a result of large prediction error; the two activities of the ACC populations increased afterwards, as the latent variable z gradually increased. Right after withdrawal, S1 population firing decreased immediately, while ACC population firing decayed slower. Throughout the trial, the ACC population that received S1 inputs had a greater firing intensity than the ACC population that did not.

We computed time-averaged pre-S1 synaptic activation and post-ACC synaptic activation (Methods). By varying the stimulus amplitude, we ran 50 Monte Carlo simulations and found that the result was consistent with the previous empirical model, showing a relatively weak correlation for evoked pain (Fig. 7C).

Spontaneous pain. In the spontaneous pain condition, we set $a = 2000$, $Z_{\text{threshold}} = 400$. As shown in Fig. S2, the firing rate of both S1 and ACC populations increased with a similar pace when the initial top-down expectation $z(0)$ was set to a positive value. We computed the pre-S1 and post-ACC activity by varying the initial value of z, and found a strong positive correlation between them (Fig. 7D), which is consistent with experimental results, as well as our empirical model (Fig. 4E).

Placebo condition. To simulate the placebo effect, we set a negative $z(t)$ to represent a biased subjective pain perception. In the placebo condition, we set $a = 2000$, $Z_{\text{threshold}} = 500$, and the initial top-down expectation as a negative value. The pulse input has a 200-ms duration. As presented in Fig. S3, the existence of a negative z produced a large prediction error, driving the S1 population to increase the firing rate, while suppressing the firing of ACC population. After the onset of stimulus, the S1 firing rate increased quickly, while the firing rate increase in the ACC population was slower. By varying the initial value of z, we found a negative correlation between pre-S1 and post-ACC power (Fig. 7E), in line with the result derived from the empirical model (Fig. 4G).

Within the predictive coding framework, placebo-induced treatment expectations can be conceptualized as feedback-mediated predictions, which modulate pain by

changing the balance of feedback and feedforward processes at different levels of a neural processing hierarchy [43].

Chronic pain. To simulate the chronic pain condition, we considered three experimental phenomena observed in chronic pain: the increasing percentage of ACC neurons that receive S1 input, the increasing percentage of pain-responsive neurons in each ACC subpopulation, and the activation of S1→ACC pathway (A. Singh, unpublished data). We focused on the targeted ACC neuron population. Specifically, we increased the percentage of ACC neurons that receive direct S1 input from 20% to 30%, increased the scaling parameter q_{S1^+} from 35% to 60%, q_{S1^-} from 14% to 20%, and q_I from 10% to 25%, and increased L from 0.1 to 0.2. Other model parameters were kept unchanged as before (see Fig. 8A).

In the evoked pain condition, we first computed the traces of synaptic variable s in single-trial simulations. As expected, with a relatively low stimulus ($x = 3.0$), the ACC population had a significantly higher firing intensity in the chronic pain condition than in the naive case (Fig. 8B). When the stimulus was sufficiently high ($x = 4.0$), the ACC population had a similar firing intensity in both chronic and naive situations (Fig. 8C).

Next, by varying the stimulus amplitude from 1.3 to 5.0, we ran 100 trials and computed the averaged synaptic variable s of the ACC population from the stimulus onset to withdrawal, which reflects the overall firing intensity of ACC neurons in response to the stimulus. As presented in Fig. 8D, the difference in firing intensity between naive and chronic pain conditions increased with the increasing stimulus amplitude in the presence of low-intensity stimulus; this difference diminished with increasing stimulus amplitude in the presence of high-intensity stimulus. With chronic pain, the ACC firing intensity increased disproportionally depending on the stimulus intensity, which is consistent with our previous experimental findings [7]. In addition, we have also computed the maximum synaptic activation as well as the latency to the maximum (Fig. S4).

We then considered the activities of ACC subpopulations $E_{2\text{-}1}$ and $E_{2\text{-}2}$ separately. As shown in Fig. 8E at low-intensity stimulus, the response of the ACC subpopulation with S1 input was similar to the total population's, showing a significant increase in firing rate from naive to chronic pain. However, the ACC subpopulation without

receiving the S1 input did not change their firing significantly (Fig. 8F). This indicated that the disproportional increase in ACC firing intensity from naive to chronic pain was contributed mainly by neurons that received the S1 input. It is noticeable that under high-intensity stimulus, when the difference in firing between naive and chronic was small for the ACC subpopulation with the S1 input, but this difference was significant for the ACC subpopulation without the S1 input, as shown in Fig. 8G). Interestingly, we found that the firing of subpopulation $E_{2\text{-}2}$ was suppressed under the chronic pain condition.

Experimentally, we have found the ACC baseline firing rate is higher in chronic pain than the naive condition (A. Singh, unpublished data). Our model prediction also supported this finding (Fig. 8H), where the time-average of ACC baseline activity was computed over the period $[0.5, 1.5]$ s.

In the absence of stimulus, we found that chronic pain induces more sustainable high firing intensity in the ACC. We computed the fraction of time when s was greater than a certain threshold within the period T_s (from z onset to withdrawal), and found a sigmoid-like shape with increasing $z(0)$ (Fig. 9C). From naive to chronic pain, the sigmoid curve shifted toward the left, which indicated that the fraction of time saturated at a lower z level in the chronic pain condition. As shown in Fig. 9A, when z was low, chronic pain induced a higher and sustainable firing response compared with the naive condition. when z was high, both curve saturated so the time above threshold was nearly the same in both conditions (Fig. 9B). This implies that if spontaneous pain was primarily induced by a top-down input, then the nociceptive response of ACC neurons in spontaneous pain under chronic pain would be more sustainable than that in naive case.

In the placebo/nocebo condition, we found a monotonically increasing trend in ACC firing with respect to increasing z in both naive and chronic pain conditions (Fig. 9D), where negative $z(0)$ corresponded to the placebo effect and positive $z(0)$ to the nocebo effect. This is consistent with the definitions of placebo effect as reduced nociceptive responses and the nocebo effect as increased responses. We also found that the curve shifted upward from naive to chronic pain condition, indicating that the placebo effect was weaker (i.e., feeling less relieved) and the nocebo effect was stronger (i.e., feeling more painful) in chronic pain. The mean firing curve of each subpopulation with regard

to $z(0)$ (Fig. 9E) demonstrated that the ACC subpopulation receiving the S1 input contributed predominantly to this shift.

Precise noxious stimulus prediction decreases the S1 response. We first fixed x and investigate how the S1 firing intensity would change in respect to different $z(0)$. As shown in Fig. 10A, the pre-stimulus S1 firing intensity increased monotonically with $z(0)$. However, the post-stimulus S1 firing intensity was determined by the PE, or $|x - z(0)|$. As shown in Fig. 10B, the curve of post-stimulus S1 firing intensity had a V-shape with regard to $z(0)$, and the minimum of V-shape curve shifted rightward when we increased the stimulus amplitude x.

We further investigated the effect of prediction on the S1 firing intensity. We set a positive $z(0)$ and assumed that z remained constant before the stimulus onset, which represented a prediction of the stimulus x. We tested two scenarios: one with zero PE (i.e., $z(0) = x$), the other with a PE of x (i.e., $z(0) = 0$). We measured the firing intensity of pre- and post-stimulus S1 excitatory population, respectively. As illustrated in Fig. 10C, when PE was x, the pre-stimulus S1 firing was significantly lower than the post-stimulus S1 firing; however, the trend was reversed when there was a precise prediction (i.e. PE=0).

Our mean field model prediction is in line with several experimental findings in the literature. First, human S1 gamma oscillations can predict subjective pain intensity (but not objective stimulus intensity) [44, 45]. Second, the precise prediction of pain stimulus intensity decreases gamma-band activity [10]. Third, the prediction level is positively correlated with the "rating" of pain stimulus [46].

Discussion

Neural pathways for pain perception

In the paper, we have only focused our attention on the S1 and ACC circuits in the context of predictive coding. In reality, however, many more cortical or subcortical circuits are engaged in pain processing. In the ascending ("bottom-up") pathway, the nocioception originates in the peripheral system, and then passes the signals to the dorsal horn of the spinal cord, then further to the thalamus, and the cortex. The

descending ("top-down") system, involving the midbrain, RVM (rostral ventromedial medulla), PAG (periaqueductal gray) and other areas, can exert both inhibitory and modulatory influence. There may be multiple routes of descending control. It may originate in the cortex, including the ACC, and project to the PAG. The PAG in turn sends projections to RVM and then to the spinal cord [43].

Several lines of experimental evidence have pointed to a direct S1→ACC projection in cortical pain processing [22, 27, 28]. To date, however, it remains unknown whether there is an indirect ACC→S1 pathway through the cortico-cortical feedback loop that modulate pain processing. More experimental investigations are still required in the future. At the computational side, we have tried incorporating ACC→S1 feedback into the mean field model, and found qualitatively similar observations in the average S1 synaptic activation variable as the case without feedback (Fig. S5).

The ACC is a major target of midbrain dopamine neurons, which encode reward-related information (such as the reward prediction error). The ACC is reciprocally connected with the amygdala and the orbitofrontal cortex (OFC), which has a projection to the nucleus accumbens (NAc). Importantly, the ACC is also reciprocally connected with the prefrontal cortex (PFC), a region implicated in executive control, working memory, and rule learning. Therefore, the ACC may serve as a gateway for incorporating reward-related information into sensorimotor mappings subserved by the PFC [47]. Moreover, the PFC has been confirmed to play a modulatory role of gain control in pain processing [25]. Activation of the PFC provides effective relief to sensory and affective pain symptoms via descending projections in rodents [48–51]. Nevertheless, a complete circuit dissection of cortical pain processing between sensory cortices, ACC, OFC, and PFC has not been achieved.

Experimental evidence for predictive coding in pain perception

In the presence of uncertainties, the brain uses a prediction strategy to guide decision making or perceptual inference. Within the predictive coding theory, oscillatory beta-band activity has been linked to top-down prediction signals and gamma-band activity to bottom-up prediction errors [52]. Specifically, in a human MEG study, Granger-causal connectivity in the beta-band was found to be strongest for backward

top-down connections, whereas the gamma-band was found to be strongest for feed-forward bottom-up connections [52].

Predictive coding can provide the key to understanding important phenomena in pain perception [8, 11, 53]. Unlike evoked pain that is elicited by external noxious stimuli, spontaneous pain is detached from an overt stimulus and may be driven by internal processing inside the pain matrix. A statistically significant finding from our previous experimental data [26] is the fact that the pre-S1 gamma-ERD/ERS correlates with the post-ACC beta-ERS/ERD during spontaneous pain, whereas the correlation becomes weaker or diminishes in evoked pain or baseline (Fig. 1C,D). This phenomenon holds for both naive and chronic pain-treated rats, suggesting an information flow between the bottom-up (gamma) and top-down (beta) loops. Therefore, for the purpose of predictive coding, the brain may use differential neuronal responses to represent bottom-up and top-down modulations of pain, and to provide complementary information about pain perception [54].

The temporal coordination of beta-ERS/ERD and gamma-ERD/ERS between the ACC and S1 during pain perception collaborates with some previous gamma-ERS and alpha or beta-ERD reports on human EEG findings [44, 55, 56]. The pain-induced alpha or beta-ERS/ERD is highly dependent on the cortical region, which may be related to sensory gating and functional inhibition, or influenced by top-down attention modulation [46]. In addition, it has been reported that pre-stimulus human EEG oscillations in the alpha (at bilateral central regions) and gamma (at parietal regions) bands negatively modulated the perception of subsequent nociceptive stimuli [57].

Chronic pain

In the chronic pain state, sensory hypersensitivity and aversion are commonly observed. Chronic pain can alter acute pain intensity representations of noxious stimuli in the ACC to induce generalized enhancement of aversion [7]. While cortical pain responses differ between naive and chronic pain animals, the exact mechanisms of transitioning from acute to chronic pain is still incompletely understood. Our computational model can provide valuable predictions to confirm the experimental findings.

In chronic pain experiments, CFA mice with inflammatory pain show elevated

resting gamma and alpha activity and increased gamma power in response to sub-threshold stimuli, in association with nociceptive hypersensitivity. Inducing gamma oscillations via optogenetic activation of parvalbumin-expressing inhibitory interneurons in the S1 enhances nociceptive sensitivity and induces aversive avoidance behavior [58]. In addition, the magnitude of placebo analgesia effect appears to be strong in chronic pain patients experiencing hyperalgesic states [59]. Our simulation results have indirectly supported these findings (Fig. 8 and Fig. 9, respectively).

In summary, motivated by prior experimental findings, we have developed a predictive coding framework and computational models to characterize the neuronal population activity of the rat S1 and ACC during various pain conditions (evoked, spontaneous and chronic pain). The empirical model is phenomenological and aimed to characterize the macroscopic neural activity, whereas the mean field model is mechanistic and aimed to characterize the mesoscopic neuronal population activity. Importantly, our mean field model imposes biological constrains onto the E/I populations. Although our computational models have presented a good characterization or prediction of the animal data, it would be interesting to further validate the predictive coding theory extensively in human pain experiments. This would require the use of source localization techniques for reconstructing the S1 and ACC activity based on high-density EEG or MEG recordings [52, 60, 61]. In addition, our computational model may provide predictions for other experimental conditions, such as investigating cortical pain processing during pain perception in the presence of anesthetic or analgesic drugs [62].

Acknowledgments

Preliminary version of this work was presented in Proceedings of IEEE EMBC'19, Berlin, July 23-28, 2019 [63].

Funding: This work was partially supported by the NSF-CBET grant 1835000 (ZSC, JW), NIH R01-NS100065 (ZSC, JW), R01-MH118928 (ZSC), R01-GM115384 (JW), and a fellowship of the NIH Training Program in Computational Neuroscience (HK) supported by NIH T90/R90 DA043219 and DA043849. The funders had no role in study design, data collection and analysis, decision to publish, or preparation of the manuscript.

Data Availability: All data analysis and simulation software files are available at https://github.com/yuru-eats-celery/pain-coding-model and https://github.com/ymch815/predictive-coding-mean-field-model.git

Author Contributions

Conceived and designed the experiments: ZSC, JW. Supervised the project: ZSC. Performed the experiments and collected the data: QZ, ZX, AS. Analyzed the data: YS, MY, HK, ZX. Contributed the software: YS, MY, AB. Wrote the paper: ZSC.

References

1. Bushnell MC, Duncan GH, Hofbauer RK, Ha B, Chen JI, Carrier B. Pain perception: is there a role for primary somatosensory cortex? *Proc. Natl. Acad. Sci. USA* 1999; 96: 7705-7709.

2. Bushnell MC, Ceko M, Low LA. Cognitive and emotional control of pain and its disruption in chronic pain. Nat. Rev. Neurosci. 2013; 14: 502–511.

3. Iannetti GD, Mouraux A (2010). From the neuromatrix to the pain matrix (and back). Exp. Brain Res. 2010; 205: 1–12.

4. Legrain V, Iannetti GD, Plaghki L, Mouraux A. The pain matrix reloaded: a salience detection system for the body. Progress in Neurobiology 2011; 93: 111–124.

5. Vierck CJ, Whitsel BL, Favorov OV, Brown AW, Tommerdahl M. Role of primary somatosensory cortex in the coding of pain. PAIN 2013; 154: 334–344.

6. Johansen JP, Fields HL, Manning BH. The affective component of pain in rodents: direct evidence for a contribution of the anterior cingulate cortex. Proc. Natl. Acad. Sci. USA 2001; 98: 8077–8082.

7. Zhang Q, Mander TR, Tong APS, Yang R, Garg A, Martinez E, Zhou H, Dale J, Goyal A, Urien L, Yang G, Chen Z, Wang J. Chronic pain induces generalized enhancement of aversion. eLife 2017; 6: e25302.

8. Wiech K. Deconstructing the sensation of pain: the influence of cognitive processes on pain perception. Science 2016; 354: 584–587.

9. Bennett GJ. What is spontaneous pain and who has it? J. Pain 2012; 13: 921–929.

10. Arnal LH, Giraud AL (2012). Cortical oscillations and sensory predictions. Trends Cogn. Sci. 2012; 16: 390–398.

11. Ploner M, Sorg C, Gross J. Brian rhythms of pain. Trends Cog. Sci. 2017; 21: 100–110.

12. Huang Y, Rao RPN. Predictive coding. Wiley Interdiscip. Rev. Cogn. Sci. 2011; 2: 580-593.

13. Aitchison L, Lengyel M. With or without you: predictive coding and Bayesian inference in the brain. Curr. Opin. Neurobiol. 2017; 46: 219–227.

14. Rao RP, Ballard DH. Predictive coding in the visual cortex: a functional interpretation of some extra-classical receptive-field effects. *Nature Neurosci.* **2**, 79–87.

15. Shipp S, Adams RA, Friston KJ. Reflections on agranular architecture: predictive coding in the motor cortex. Trends Neurosci. 2013; 36: 706–716.

16. Talsma D. Predictive coding and multisensory integration: an attentional account of the multisensory mind. Front. Integrative Neurosci. 2015: 9: 19.

17. Sedley W, Gander PE, Kumar S, et al. Neural signatures of perceptual inference. eLife 2016; 5: e11476.

18. Bastos AM, Usrey WM, Adams RA, Mangun GR, Fries P, Friston KJ. Canonical microcircuits for predictive coding. Neuron 2012; 76: 695–711.

19. Friston KJ, Kiebel S (2009). Predictive coding under the free-energy principle. Philosophical Transactions of the Royal Society B: Biological Sciences 2009; 364: 1211–1221.

20. Friston KJ, Bastos AM, Pinotsis D, Litvak V. LFP and oscillations–what do they tell us? Curr. Opin. Neurobiol. 2015; 31: 1–6.

21. Peng W, Xia X, Yi M, Huang G, Zhang Z, Iannetti G, Hu L. Brain oscillations reflecting pain-related behavior in freely moving rats. PAIN 2018; 158: 106–118.

22. Eto K, Wake H, Watanabe M, et al. Inter-regional contribution of enhanced activity of the primary somatosensory cortex to the anterior cingulate cortex accelerates chronic pain behavior. J. Neurosci. 2011; 31: 7631–7636.

23. Bressler SL, Richter CG. Interareal oscillatory synchronization in top-down neocortical processing. Curr. Opin. Neurobiol. 2015; 31: 62–66.

24. Urien L, Xiao Z, Bauer EP, Chen Z, Wang J. Rate and temporal coding mechanisms in the anterior cingulate cortex for pain anticipation. Sci. Rep. 2018; 8: 8298.

25. Dale J, Zhou H, Zhang Q, Martinez E, Hu S, Liu K, Urien L, Chen Z, Wang J. Scaling up cortical control inhibits pain. Cell Rep. 2018; 23: 1301-1313.

26. Xiao Z, Martinez E, Kulkarni P, Zhang Q, Rosenberg D, Hou Q, Zhou H, Wang J, Chen Z. Cortical pain processing in the rat anterior cingulate cortex and primary somatosensory cortex. Front. Cellular Neurosci. 2019; 13: 165.

27. Sesack SR, Deutch AY, Roth RH, Bunney BS. Topographical organization of the efferent projections of the medial prefrontal cortex in the rat: an anterograde tract-tracing study with Phaseolus vulgaris leucoagglutinin. J Comp. Neurol. 1989; 290: 213–242.

28. Sesack SR, Pickel VM. Prefrontal cortical efferents in the rat synapse on unlabeled neuronal targets of catecholamine terminals in the nucleus accumbens

septi and on dopamine neurons in the ventral tegmental area. J Comp. Neurol. 1992; 320: 145–160.

29. Pinotsis D, Robinson P, Graben PB, Friston K. Neural masses and fields: modeling the dynamics of brain activity. Front. Comput. Neurosci. 2014; 8: 149.

30. Wilson HR, Cowan JD. Excitatory and inhibitory interactions in localized populations of model neurons. Biophysics Journal 1972; 12: 1–24.

31. Ermentrout GB, Cowan JD. A mathematical theory of visual hallucination patterns. Biol. Cyber. 1979; 34: 137–150.

32. Bressloff PC, Cowan JD, Golubitsky M, Thomas PJ, Wiener MC. Geometric visual hallucinations, Euclidean symmetry and the functional architecture of striate cortex. Philosophical Transactions of the Royal Society of London. Series B, Biological Sciences 2001; 356: 299–330.

33. Wilson HR, Blake R, Lee SH. Dynamics of traveling waves in visual perception. Nature 2011; 412: 907–910.

34. Shusterman V, Troy WC. From baseline to epileptiform activity: a path to synchronized rhythmicity in large-scale neural networks. Phys. Rev. E 2008; 77: 061911.

35. Meijer HGE, Eissa TL, Kiewiet B, Neuman JF, Schevon CA, Emerson RG, Goodman RR, McKhann GM, Marcuccilli CJ, Tryba AK, Cowan JD, van Gils SA, van Drongelen W. Modeling focal epileptic activity in the Wilson-Cowan model with depolarization block. J. Math. Neurosci. 2015; 5: 7.

36. Deco G, Jirsa VK, McIntosh AR. Emerging concepts for the dynamical organization of resting-state activity in the brain. Nature Rev. Neurosci. 2011; 12: 43–56.

37. Roberts JA, Gollo LL, Abeysuriya RG, Roberts G, Mitchell PB, Woolrich MW, Breakspear M. Metastable brain waves. Nat. Commun. 2019; 10: 1–17.

38. Lea-Carnall CA, Montemurro MA, Trujillo-Barreto NJ, Parkes LM, El-Deredy W. Cortical resonance frequencies emerge from network size and connectivity. PLoS Comp. Biol. 2016; 12: 1–19.

39. Keeley S, Byrne A, Fenton A, Rinzel J. Firing rate models for gamma oscillations. J. Neurophysiol. 2019; 121: 2181–2190.

40. Deuis JR, Dvorakova, LS, Vetter I. Methods used to evaluate pain behaviors in rodents. Front. Molecular Neurosci. 2017; 10: 284.

41. Dirig DM, Salami A, Rathbun ML, Ozaki GT, Yash TL. Characterization of variables defining hindpaw withdrawal latency evoked by radiant thermal stimuli. J. Neurosci. Methods 1997; 76: 183–191.

42. Wagner TD, Atlas LY. The neuroscience of placebo effects: connecting context, learning and healthy. Nat. Rev. Neurosci. 2015; 16: 403–418.

43. Buchel C, Geuter S, Sprenger C, Eippert F. Placebo analgesia: a predictive coding perspective. Neuron 2014; 81:1223–1239.

44. Gross J, Schnizler A, Timmermann L, Ploner M. Gamma oscillations in human primary somatosensory cortex reflect pain perception. PLoS Biol. 2007; 5: e133.

45. Zhang ZG, Hu L, Hung YS, Mouraux A, Iannetti GD. Gamma-band oscillations in the primary somatosensory cortex—a direct and obligatory correlate of subjective pain intensity. J. Neurosci. 2012; 32: 7429–7438.

46. Peng W, Babiloni C, Mao Y, Hu Y. Subjective pain perception mediated by alpha rhythms. Biol. Psychol. 2015; 109: 141–150.

47. Hayden BY, Platt ML. Cingulate cortex. In Encyclopedia of Neuroscience (Elsevier, 2009).

48. Lee M, et al. Activation of corticostriatal circuitry relieves chronic neuropathic pain. J. Neurosci. 2015; 35: 5247–5259.

49. Martinez, E., et al. Corticostriatal regulation of acute pain. Front. Cell. Neurosci. 2017; 11: 146.

50. Zhang Z, et al. Role of prelimbic GABAergic circuits in sensory and emotional aspects of neuropathic pain. Cell Rep. 2015; 12: 752–759.

51. Hardy, S.G. Analgesia elicited by prefrontal stimulation. Brain Res. 1985; 339: 281–284.

52. van Pelt S, Heil L, Kwisthout J, Ondobaka S, van Rooij I, Bekkering H. Beta and gamma-band activity reflect predictive coding in the processing of causal events. Soc. Cog. Affect Neurosci. 2016; 11: 973–980.

53. Morrison I, Perini I, Dunham J. Facets and mechanisms of adaptive pain behavior: predictive regulation and action. Front. Hum. Neurosci. 2013; 7: 755.

54. Tiemann L, May ES, Postorino M, Schulz E, Nickel MM, Bingel U, Ploner M. Differential neurophysiological correlates of bottom-up and top-down modulations of pain. PAIN 2015; 156: 289–296.

55. Hu L, Peng W, Valntini E, Zhang Z, Hu Y. Functional features of nociceptive-induced suppression of alpha band electroencephalographic oscillations. J. Pain 2013; 14: 89–99.

56. Schultz E, May ES, Tiemann L, Nickel MM, Witkovsky V, Schmidt P, Gross J, Ploner M. Prefrontal gamma oscillations encode tonic pain in humans. Cereb. Cortex 2015; 25: 4407–4414.

57. Tu Y, Zhang Z, Tan A, et al. Alpha and gamma oscillation amplitudes synergistically predict the pereption of forthcoming nociceptive stimuli. Hum. Brain Mapp. 2016; 37: 501–514.

58. Tan LL, Oswald MJ, Heinl C, et al. Gamma oscillations in somatosensory cortex recruit prefrontal and descending serotonergic pathways in aversion and nociception. Nat Commun. 2019; 10: 983.

59. Vase L, Petersen GL, Lund K. Placebo effects in idiopathic and neuropathic pain conditions. In Benedetti F, Enck P, Frisaldi E, Schedlowski M (eds). *Placebo* (pp. 121–136). Springer (2014).

60. Hauck M, Domnick C, Lorenz J, Gerloff C, Engel AK. Top-down and bottom-up modulation of pain-induced oscillations. Front. Hum. Neurosci. 2015; 9: 375.

61. Zhang CH, Sohrabpour A, Lu Y, He B. Spectral and spatial changes of brain rhythmic activity in response to the sustained thermal pain stimulation. Hum. Brain Mapp. 2016; 37: 2976–2991.

62. Zhou H, Zhang Q, Martinez E, Hu S, Liu K, Dale J, Huang D, Yang G, Chen Z , Wang J. Ketamine reduces hyperactivity of the anterior cingulate cortex to provide enduring relief of chronic pain. Nat. Commun. 2018; 9: 3751.

63. Song Y, Kemprecos H, Wang J, Chen Z. A predictive coding model for evoked and spontaneous pain. Proc. IEEE EMBC. 2019; pp. xxx.

Supporting Information

S1 Fig. Comparison of firing rate variable r and synaptic activation variable s in evoked pain based on the mean field model. (**A**) Representative simulated traces of firing rate (red) and synaptic activation (blue) of ACC population $E_{2\text{-}1}$ in one evoked pain trial. Dashed lines show the upper and lower envelope of the oscillation. (**B**) Replot the midline of the envelopes in panel A. (**C**) Scatter plot of firing rate variable and synaptic activation variable in panel A. Two variables are highly correlated (Spearman's correlation 0.969, $p < 10^{-10}$).

S2 Fig. Mean-field activity (synaptic current s) for three different excitatory populations in one simulation of spontaneous pain. Notations are the same as Fig 7A,B.

S3 Fig. Mean-field activity (synaptic current s) for three different excitatory populations in one simulation of placebo condition. Notations are the same as Fig 7A,B.

S4 Fig. Latency and maximum peak statistics of ACC synaptic activation during evoked pain (A-D), spontaneous pain (E-H) and placebo/nocebo (I-L) conditions. (**A**) Maximum of middle line of ACC synaptic activation variable s from total population during the duration T_s between the stimulus onset to withdrawal, for varying stimulus amplitude under naive (blue) and chronic pain (red) condition. (**B**) Similar to panel C, except for two ACC subpopulations. All curves have a linearly decreasing shape except for the population $E_{2\text{-}2}$ in chronic pain (purple), which decays exponentially. (**C**) The latency from the stimulus onset to the maximum defined in panel A for varying stimulus amplitude under the naive (blue) and chronic pain (red) conditions. The latency decay exponentially in chronic pain and linearly in the naive condition. (**D**) Similar to panel A, except for two ACC subpopulations $E_{2\text{-}1}$ (w/ S1) and $E_{2\text{-}2}$ (w/o S1). Mean and SEM for each group are shown. 100 Monte Carlo runs were run with random initial $x(0) \in [1.3, 5.0]$. (**E**) Average of middle line of ACC synaptic activation variable s from total population during the duration T_s for varying top-down expectation $z(0)$ under naive (blue) and chronic pain (red) condition. (**F**) Similar to panel E, except for two ACC subpopulations $E_{2\text{-}1}$ (w/ direct S1 input) and $E_{2\text{-}2}$ (w/o S1 input). Mean and SEM for each group are shown. 100 Monte Carlo runs were run with random initial

$z(0) \in [0.6, 3.6]$. (**G**) Maximum of middle line of ACC synaptic activation variable s from total population during the duration T_s between the stimulus onset to withdrawal, for varying top-down expectation $z(0)$ under the naive (blue) and chronic pain (red) conditions. (**H**) Similar to panel E, except for two ACC subpopulations $E_{2\text{-}1}$ (w/ direct S1 input) and $E_{2\text{-}2}$ (w/o S1). The curves in panels G and H have similar shapes as in panels E and F. (**I**) The latency from the stimulus onset to the maximum of ACC synaptic activation for varying top-down expectation $z(0)$ under naive (blue) and chronic pain (red) condition. (**J**) Similar to panel K, except for two ACC subpopulations $E_{2\text{-}1}$ (w/ direct S1 input) and $E_{2\text{-}2}$ (w/o S1). Mean and SEM for each group are shown. 100 Monte Carlo runs were run with random initial $z(0) \in [-3.0, 3.0]$. (**K**) Maximum of middle line of ACC synaptic activation variable s from total population during the duration T_s between the stimulus onset to withdrawal, for varying top-down expectation $z(0)$ under naive (blue) and chronic pain (red) condition. (**L**) Similar to panel I, except for two ACC subpopulations $E_{2\text{-}1}$ (w/ direct S1 input) and $E_{2\text{-}2}$ (w/o S1).

S5 Fig. Comparison of average S1 synaptic activation at different periods (before vs. after onset) and PE values: PE= x (or $z = 0$) and PE= 0 (or $z = x$), with feedback from ACC to S1. A total of 15 Monte Carlo trials were run with random $x(0) \in [1.8, 2.2]$. Mean and SEM were presented for each group. There was a significant difference in the average S1 synaptic activation variable between before and after stimulus in both conditions. All p-values for pairs marked in the graph are less than 0.0001, expect for the $p = 0.0138$ between PE= x and PE= 0 after onset (two pink bars). This indicates that the decrease in S1 firing intensity after stimulus onset was less significant with the presence of feedback. The firing before stimulus was computed from the expectation z onset (from 0 if no expectation) to the stimulus x onset; the firing after stimulus was computed from the stimulus onset to withdrawal. Compared to Fig. 10C, the gap between before and after stimulus was smaller here.

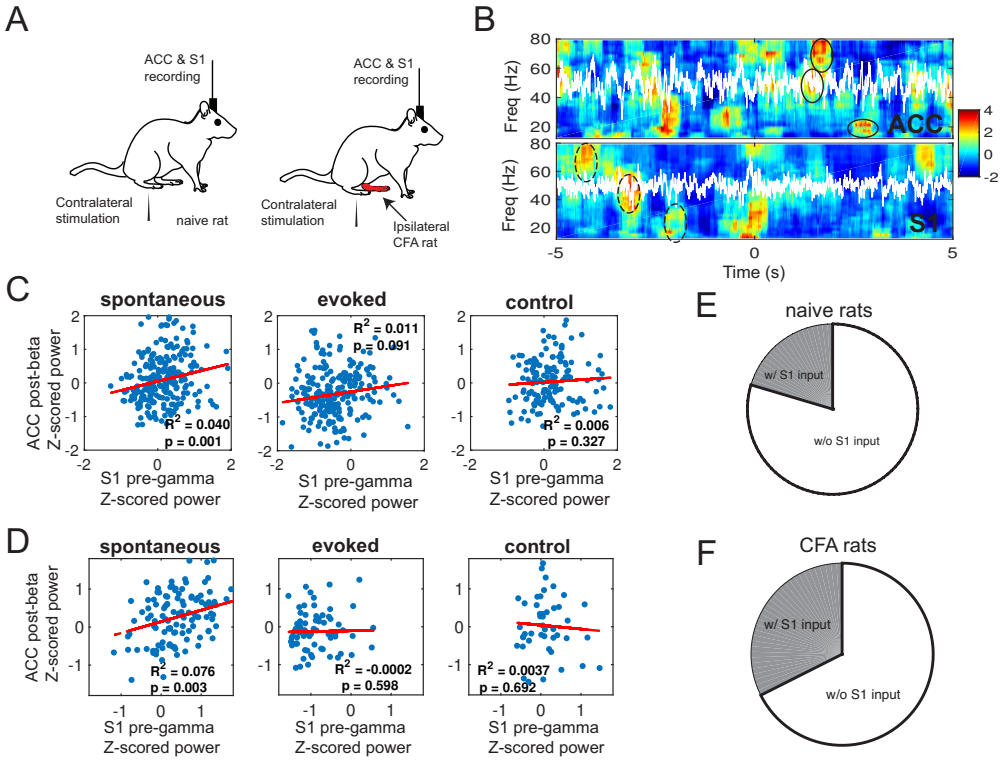

Fig 1. Results excerpted from our previous experimental findings. (**A**) Schematic diagram of noxious stimulation and electrophysiological recording in naive and CFA rats. (**B**) Z-scored spectrograms in the ACC and S1 during a representative spontaneous pain episode. White traces show the principal component of multichannel LFPs. Time 0 marks the onset of spontaneous pain event. The post-event power was Z-scored with respect to $[-5, 0]$ s, whereas the pre-event power was Z-scored with respect to $[0, 5]$ s. The S1-ERD during the pre-event period and the ACC-ERS during the post-event period were highlighted by dashed and solid ellipses, respectively. (**C**) Time-averaged Z-scored pre-γ S1 activity vs. post-β ACC activity ($n = 252$ spontaneous pain events, $n = 233$ evoked pain events; $n = 149$ negative controls). Naive rats. In each panel, R-square (i.e., the square of Pearson's correlation) and p values are reported. (**D**) Same as panel C, except for CFA rats ($n = 127$ spontaneous pain events, $n = 71$ evoked pain events; $n = 49$ negative controls). (**E**) Pie chart of pain-responsive ACC neurons that receive a direct S1 input for naive rats. (**F**) Same as panel E, except for CFA rats.

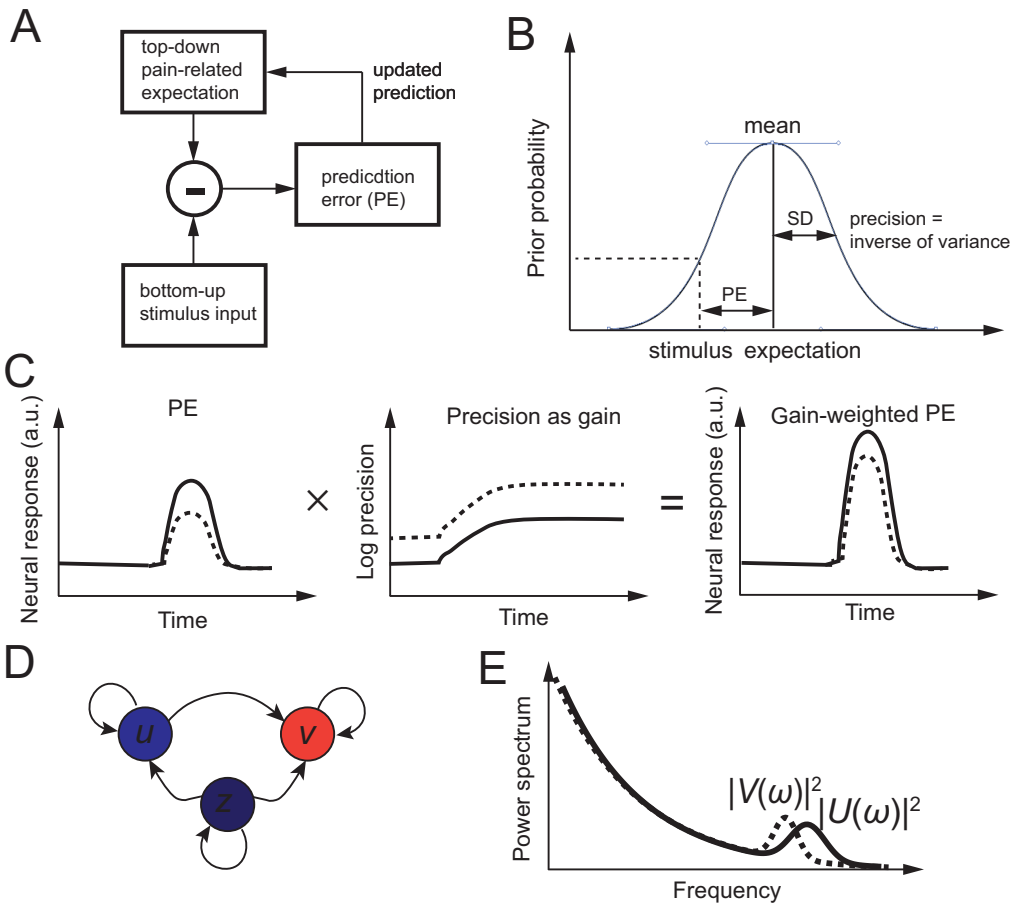

Fig 2. Predictive coding. (**A**) Schematic diagram of predictive coding for pain perception. (**B**) Graphical illustration of prediction error (PE), prior expectation, and prediction in perceptual inference. Due to the uncertainty of the top-down expectation, PE is assumed to be Gaussian distributed. Mean and standard deviation (SD) characterize the uncertainty of a Gaussian random variable. (**C**) Schematic illustration of neural response (a.u.) representing a gain-weighted PE that changes in time, where the gain is the precision statistic. (**D**) Graphical model showing statistical dependencies between the observed variables $\{u, v\}$ and the latent variable $\{z\}$ in the empirical model. (**E**) Illustration of power spectra $|U(\omega)|^2$ (solid line) and $|V(\omega)|^2$ (dashed line), where $U(\omega)$ and $V(\omega)$ are the Fourier transforms of $u(t)$ and $v(t)$ in the empirical model, respectively.

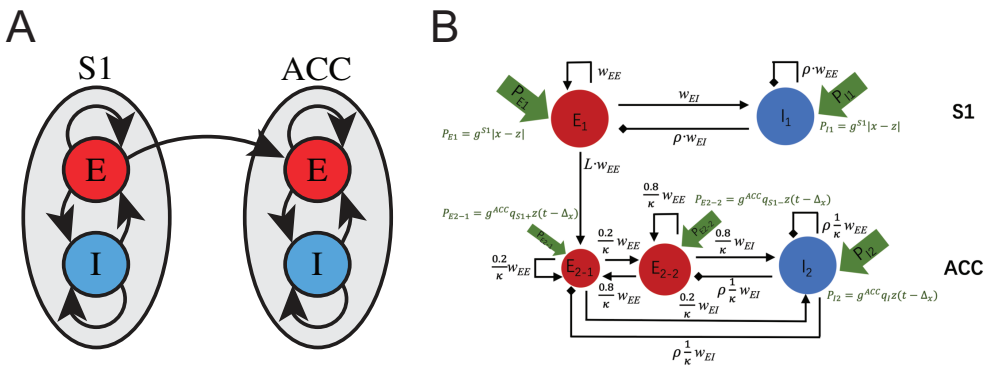

Fig 3. A schematic of computational model for the S1 and ACC circuits. (**A**) In a reduced model, each brain area is described by an excitatory (E) and an inhibitory (I) population of neurons, with inter- and intra-population coupling. The S1→ACC coupling is assumed to be excitatory and unidirectional. (**B**) A detailed mean-field model that account for biological constraints and details. The pain-responsive ACC neuronal population, $E_{2\text{-}1}$, is assumed to receive a direct excitatory input from the S1 population E_1. w_{EE} represents the basic coupling strength between the same type of neuronal populations (E-E or I-I), w_{EI} represents the basic coupling strength between different types of neuronal populations (E-I or I-E). ρ is a negative number that scales the strength of inhibitory input from I-neurons. $L < 1$ is a positive number that scales the effect of long-range S1→ACC projection. κ represents the size ratio of S1 population to ACC population.

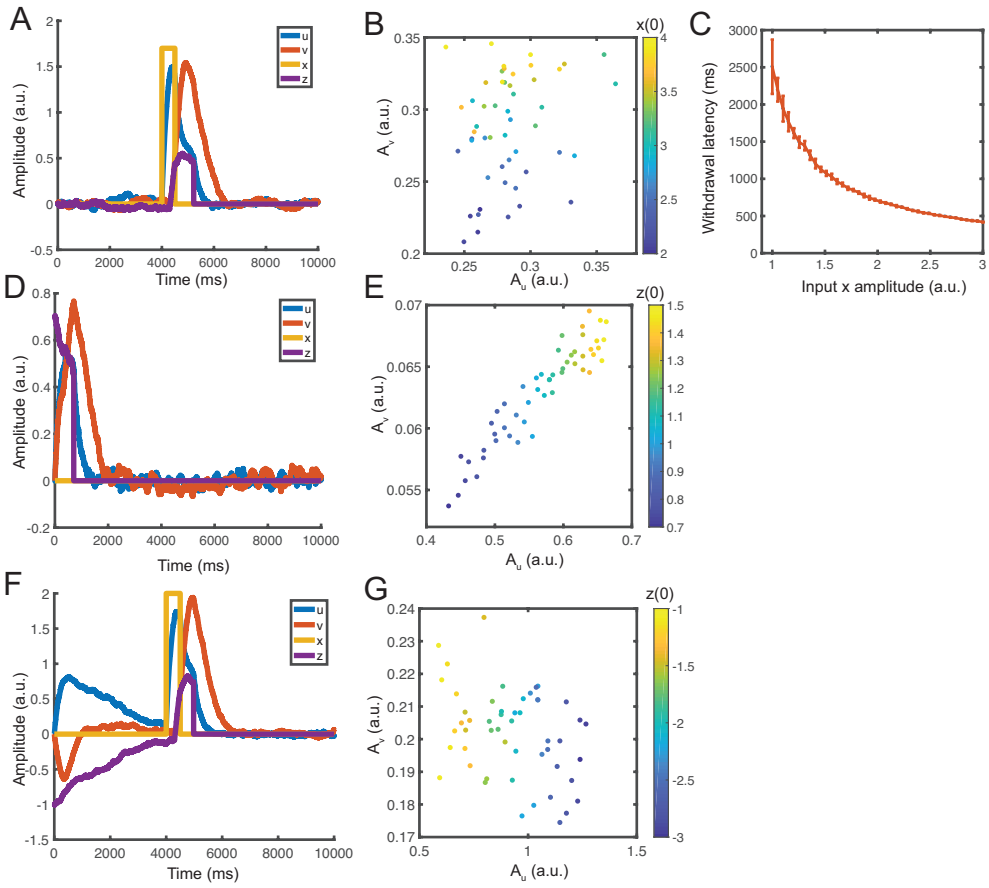

Fig 4. Simulation results from the empirical model. (**A**) Simulated 10-s temporal traces of x, z, u, v in evoked pain. Y-axis is in arbitrary unit (a.u.). Stimulus onset separates the pre-event from post-event periods. (**B**) The correlation of A_u and A_v was small during evoked pain. Each point was derived from a simulation with a different $x(0)$. Each point was derived from a simulation with a different $z(0)$. (**C**) Reset (withdrawal) latency decreases with increasing input amplitude. Error bar represents the standard error of mean (SEM) ($n = 50$). (**D**) Simulated temporal traces of x, z, u, v in spontaneous pain. Y-axis is in a.u. (**E**) A_u (during the pre-event period) was positively correlated with A_v (during the post-event period). Each point was derived from a simulation with a different $z(0)$. (**F**) Simulated temporal traces of x, z, u, v in the placebo condition. (**G**) A_u is negatively correlated with A_v. Each point was derived from a simulation with different $z(0)$.

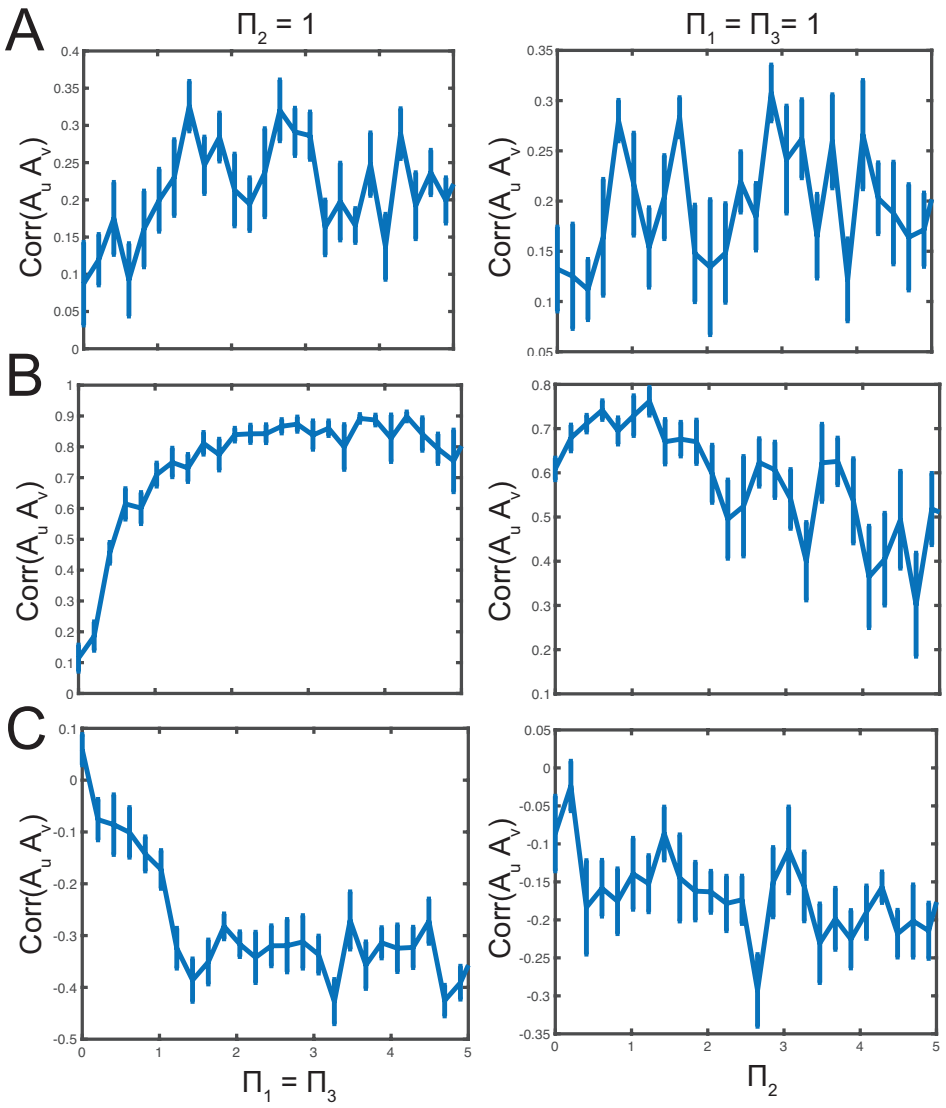

Fig 5. Sensitivity analysis of correlation between A_u and A_v with respect to the gain parameter $\{\Pi_1, \Pi_2, \Pi_3\}$ in the empirical model. (**A**) Evoked pain (**B**) spontaneous pain, (**C**) placebo condition. All error bars denote SEM ($n = 10$) and each correlation was computed from 50 trials with random initial conditions.

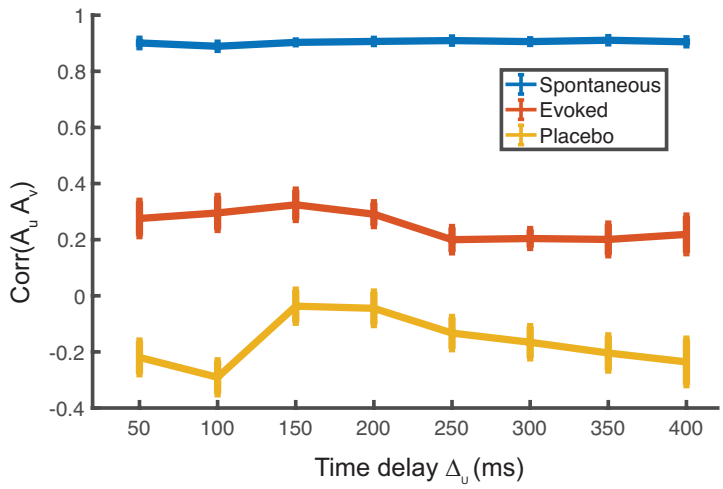

Fig 6. Sensitivity analysis of correlation between A_u and A_v with respect to the delay parameter Δ_u in the empirical model. The correlation statistics are relatively stable across a wide range of Δ_u in evoked pain (red), spontaneous pain (blue) and placebo (green) conditions. Error bar denotes SEM ($n = 10$).

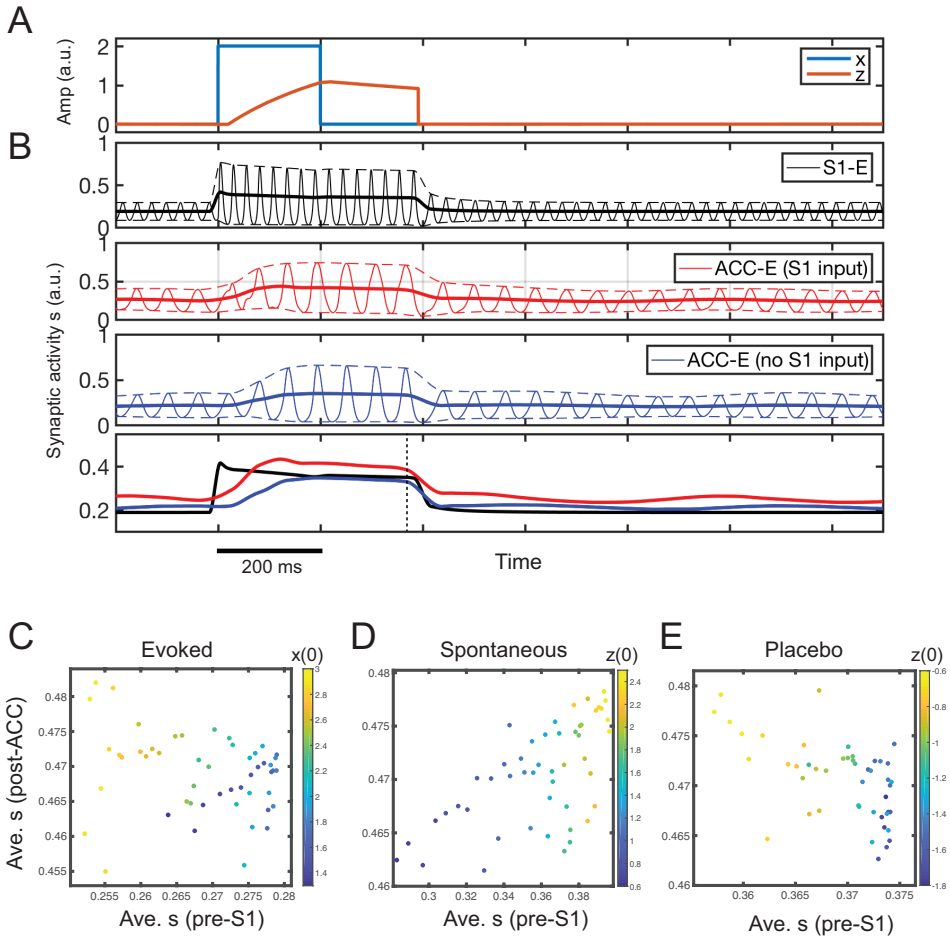

Fig 7. Simulation results from the mean field model. (**A**) Simulated stimulus input x and latent z trajectories. (**B**) Mean-field activity (synaptic activation s) for three different excitatory neuronal populations ($E_1, E_{2\text{-}1}, E_{2\text{-}2}$) in one evoke pain simulation. Dashed lines show the upper and lower bounds of the envelop around the oscillatory activity. Solid line shows the midline between the upper and lower bounds. For comparison, the last panel replots the three midlines in the first three panels. Vertical dotted line shows the onset time for post-ACC synaptic activation integration. (**C,D,E**) Scatter plots of average pre-S1 synaptic activation s versus average post-ACC synaptic activation s derived from the mean field model simulations ($n = 50$) in evoked pain, spontaneous pain and placebo condition, respectively. The Pearson's correlation coefficients in three panels were -0.239 ($p = 0.095$), 0.413 ($p = 0.0029$), and -0.529 ($p = 7.8 \times 10^{-5}$), respectively.

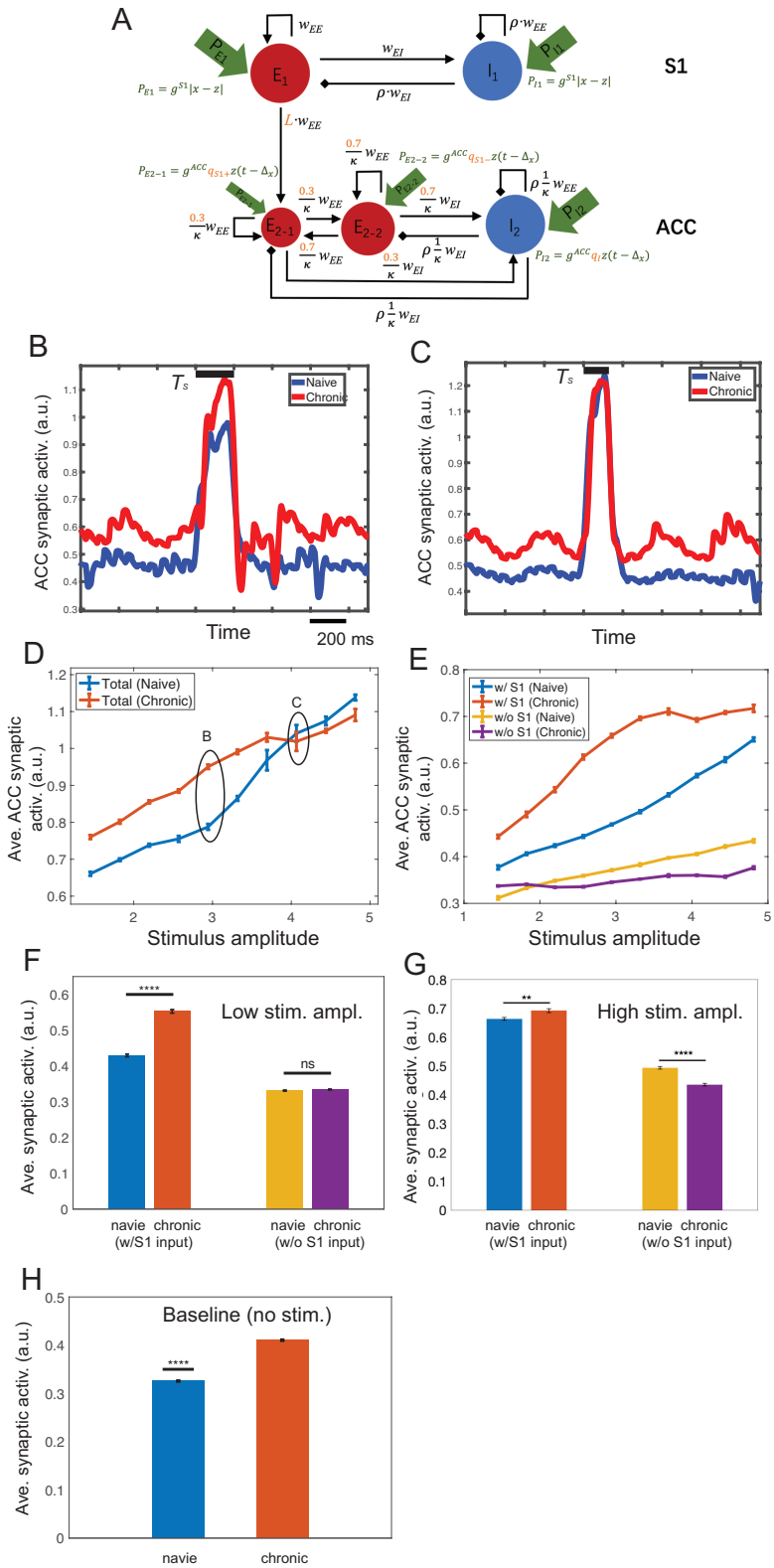

Fig 8. Mean field model simulation results of evoked pain under the chronic pain condition.

Fig 8. Mean field model simulation results of evoked pain for the chronic pain condition. (**A**) Modified mean field model (compared to Fig. 3B) for chronic pain. Modified variables are marked in red. (**B**) Comparison of the midline envelope of ACC synaptic activation variable s between naive (blue) and chronic pain (red) condition for stimulus amplitude $x(0) = 3.0$. Bar above the curve marks the duration T_s between the stimulus onset to withdrawal. (**C**) Same as panel B, except for stimulus amplitude $x(0) = 4.0$. In all following plots, the noises are set as $\epsilon_z = 0.1, \epsilon_E = \epsilon_I = 0.005$. (**D**) Average ACC synaptic activation variable s from total population during T_s for varying stimulus amplitude under naive (blue) and chronic pain (red) condition. (**E**) Similar to panel D, except for two ACC subpopulations $E_{2\text{-}1}$ (w/ direct S1 input) and $E_{2\text{-}2}$ (w/o S1). Mean and SEM for each group are shown. 100 Monte Carlo runs were run with random initial $x(0) \in [1.3, 5.0]$. (**F,G**) From panel E, we replotted the average ACC synaptic activation of $E_{2\text{-}1}$ (w/ S1) and $E_{2\text{-}2}$ (w/o S1) during T_s for low and high stimulus amplitude. Error bars were computed from 15 trials with random initial $x(0) \in [2.3, 2.7]$. For low stimulus amplitude, there was a significant difference between naive and chronic pain for $E_{2\text{-}1}$ ($p < 0.0001$, rank-sum test); but not significant for $E_{2\text{-}2}$ ($p = 0.86$). For high stimulus amplitude, there was a less significant difference between naive and chronic pain for $E_{2\text{-}1}$ ($p = 0.0082$); however, the difference of that for $E_{2\text{-}2}$ was highly significant ($p < 0.0001$). (**H**) Average ACC synaptic activation during baseline (no stimulus) was significantly lower ($p < 0.0001$, rank-sum test) in naive (blue) than in chronic pain (red). Average was computed from the baseline ([0.5, 1.5] s) by discarding the initial transient period.

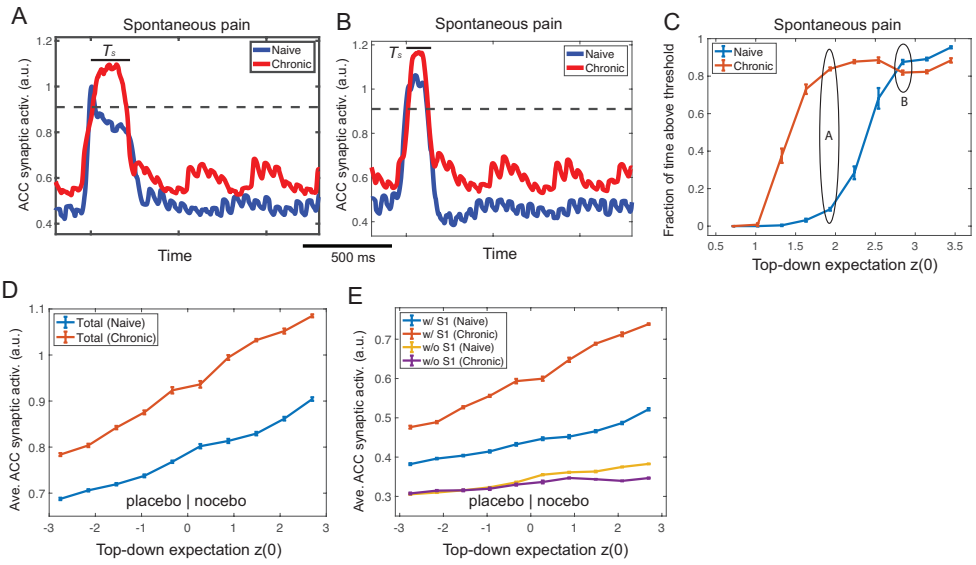

Fig 9. Mean field model simulation results of spontaneous pain and placebo/nocebo effects under the chronic pain condition. (**A**) Simulated midline envelope trace of ACC synaptic activation variable s in spontaneous pain under naive (blue) and chronic pain (red) conditions, for an initial top-down expectation $z(0) = 2.0$. (**B**) Similar to panel A, except for $z(0) = 3.0$. At low $z(0)$, the fraction of time above threshold during T_s (between the stimulus onset and withdrawal) was longer in the chronic pain condition; at high $z(0)$, the fraction was similar between the two conditions. (**C**) Fraction of time during T_s that ACC synaptic activation variable was above the threshold (horizontal dashed line) for various top-down expectation $z(0)$ in naive (blue) and chronic pain (red) conditions. The curve has a sigmoidal shape and shifts leftward from naive to chronic pain condition. 100 Monte Carlo trials were run with random $z(0) \in [0.6, 3.6]$. Mean and SEM for each group are plotted. (**D**) Comparison of average ACC synaptic activation in placebo/nocebo effects under naive (blue) and chronic pain (red) conditions for various initial top-down anticipation $z(0)$. $z(0) < 0$ and $z(0) > 0$ represent placebo and nocebo effects, respectively. The synaptic activation s of total ACC population increased monotonically, and shifted upward from naive to chronic pain condition. (**E**) Similar to panel D, except for ACC subpopulations $E_{2\text{-}1}$ (w/ S1 input) and $E_{2\text{-}2}$ (w/o S1 input). The subpopulation $E_{2\text{-}1}$ (w/ S1 input) had a similar shape of the total population, while $E_{2\text{-}2}$ (w/o S1 input) did not increase much from naive to chronic pain. 100 Monte Carlo trials were run with random $z(0) \in [-3.0, 3.0]$. Mean and SEM for each group are plotted.

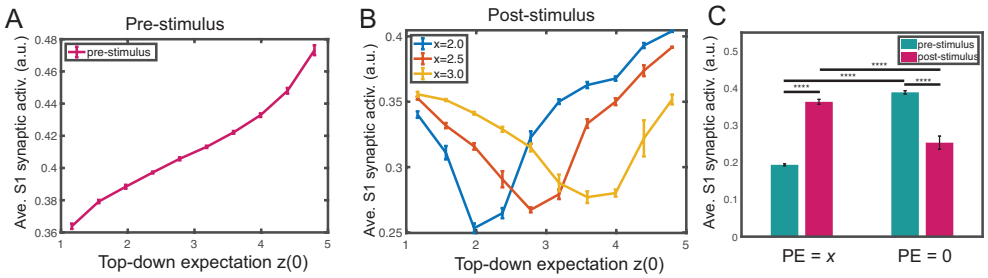

Fig 10. Mean field model simulation results of the S1 synaptic activation variable with regards to prediction error (PE) and and stimulus prediction. (**A**) During pre-stimulus baseline, time-averaged S1 synaptic activation variable increased monotonically with $z(0)$. (**B**) During post-stimulus presentation, the average S1 synaptic activation variable exhibited a V-shaped profile from varying stimulus amplitudes ($x = 2.0, 2.5, 3.0$), where the minimum occurs when $x = z(0)$ or PE $= 0$. The minimum shifted rightward with increasing x, indicating that the post-stimulus S1 synaptic activation variable was proportional to $|x - z|$ (i.e., PE). 100 Monte Carlo trials were run with random $z(0) \in [1.0, 5.0]$. Mean and SEM for each group are plotted. (**C**) Comparison of average S1 synaptic activation at different time (pre vs. post-stimulus) and PE: PE $= x$ (or $z = 0$) and PE $= 0$ (or $z = x$). 15 Monte Carlo trials were run with random $x(0) \in [1.8, 2.2]$. There was a significant difference in the average S1 synaptic activation between pre vs. post-stimulus period in both cases. All p-values for pair comparisons marked in the graph were less than 0.0001 (rank-sum test). The pre-stimulus firing was computed from the expectation z onset (from time 0 if no expectation) to the stimulus x onset; the post-stimulus firing was computed from the stimulus onset to withdrawal.

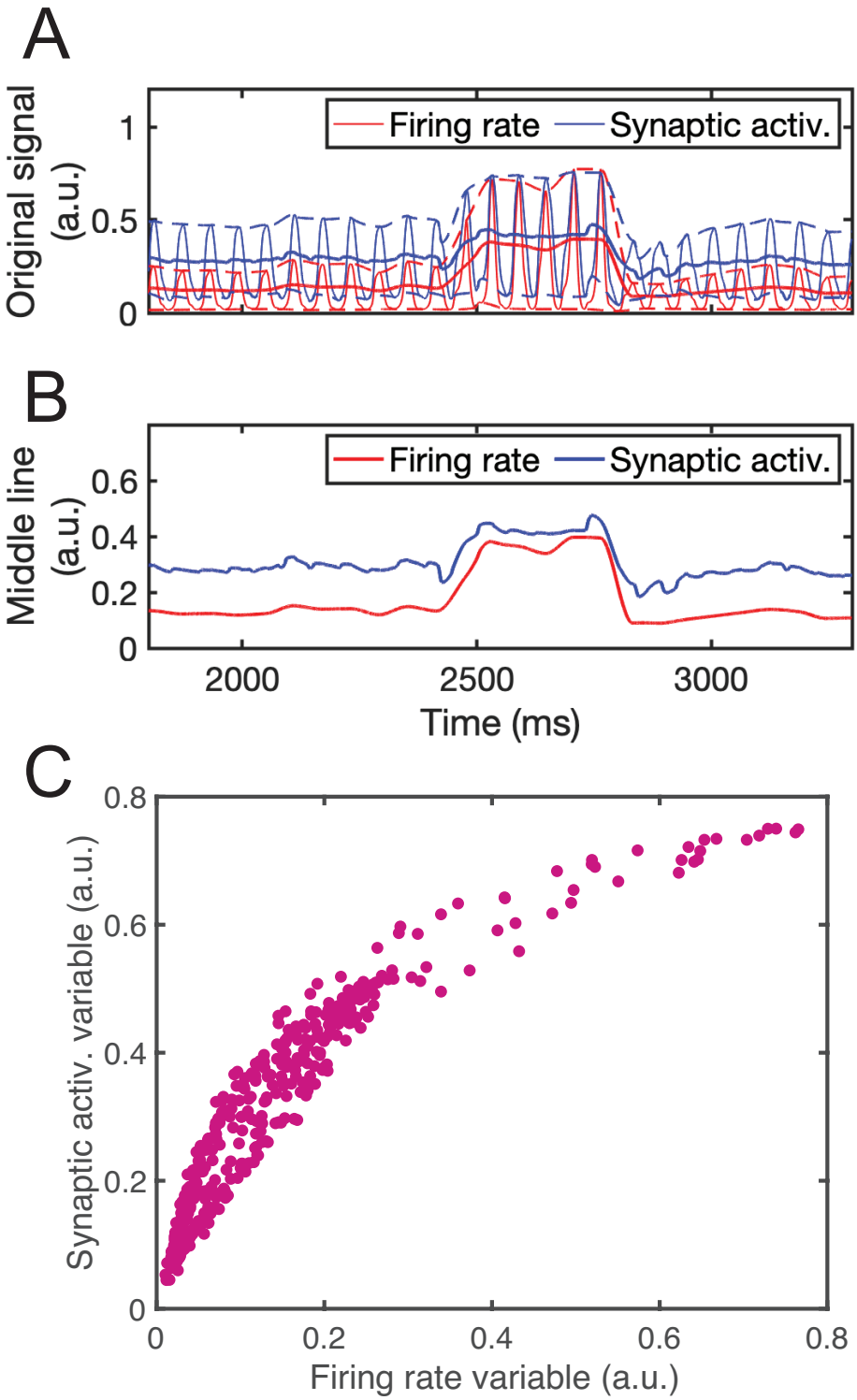

Fig S1. Comparison of firing rate variable r and synaptic activation variable s in evoked pain based on the mean field model. (**A**) Representative simulated traces of firing rate (red) and synaptic activation (blue) of ACC population $E_{2\text{-}1}$ in one evoked pain trial. Dashed lines show the upper and lower envelope of the oscillation. (**B**) Replot the midline of the envelopes in panel A. (**C**) Scatter plot of firing rate variable and synaptic activation variable in panel A. Two variables are highly correlated (Spearman's correlation 0.969, $p < 10^{-10}$).

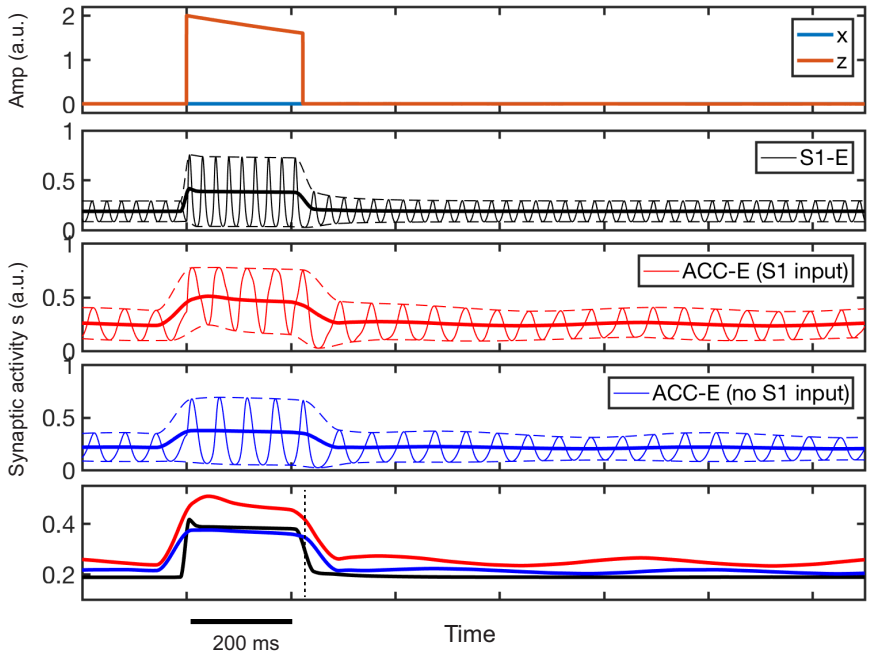

Fig S2. Mean-field activity (synaptic activation s) for three different excitatory neuronal populations in one spontaneous pain simulation. Notations are the same as Fig. 7A,B.

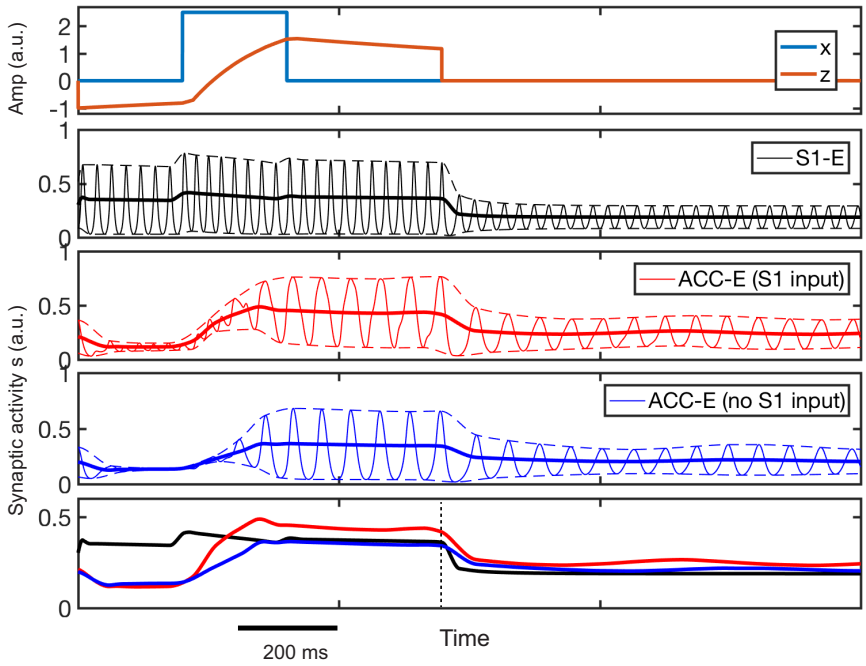

Fig S3. Mean-field activity (synaptic activation s) for three different excitatory neuronal populations in one placebo condition simulation. Notations are the same as Fig. 7A,B.

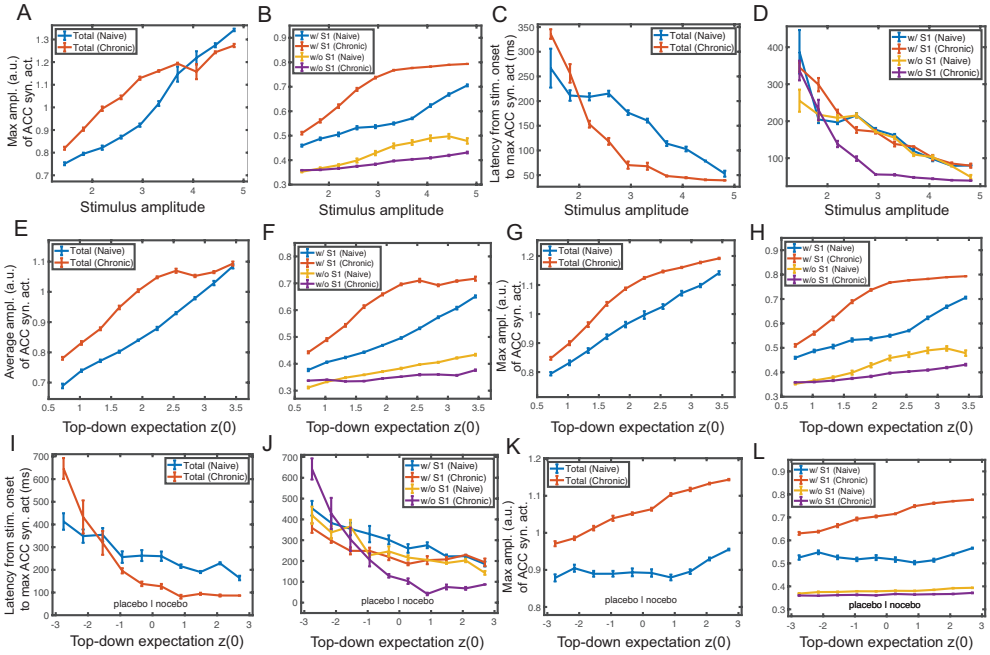

Fig S4. Latency and maximum peak statistics of synaptic activation in ACC populations during evoked pain (A-D), spontaneous pain (E-H) and placebo/nocebo (I-L) conditions. (**A**) Maximum of middle line of ACC synaptic activation variable s from total population during the duration T_s between the stimulus onset to withdrawal, for varying stimulus amplitude under naive (blue) and chronic pain (red) condition. (**B**) Similar to panel C, except for two ACC subpopulations. All curves have a linearly decreasing shape except for the population $E_{2\text{-}2}$ in chronic pain (purple), which decays exponentially. (**C**) The latency from the stimulus onset to the maximum defined in panel A for varying stimulus amplitude under the naive (blue) and chronic pain (red) conditions. The latency decay exponentially in chronic pain and linearly in the naive condition. (**D**) Similar to panel A, except for two ACC subpopulations $E_{2\text{-}1}$ (w/ S1) and $E_{2\text{-}2}$ (w/o S1). Mean and SEM for each group are shown. 100 Monte Carlo runs were run with random initial $x(0) \in [1.3, 5.0]$. (**E**) Average of middle line of ACC synaptic activation variable s from total population during the duration T_s for varying top-down expectation $z(0)$ under naive (blue) and chronic pain (red) condition. (**F**) Similar to panel E, except for two ACC subpopulations $E_{2\text{-}1}$ (w/ direct S1 input) and $E_{2\text{-}2}$ (w/o S1 input). Mean and SEM for each group are shown. 100 Monte Carlo runs were run with random initial $z(0) \in [0.6, 3.6]$. (**G**) Maximum of middle line of ACC synaptic activation variable s from total population during the duration T_s between the stimulus onset to withdrawal, for varying top-down expectation $z(0)$ under the naive (blue) and chronic pain (red) conditions. (**H**) Similar to panel E, except for two ACC subpopulations $E_{2\text{-}1}$ (w/ direct S1 input) and $E_{2\text{-}2}$ (w/o S1). The curves in panels G and H have similar shapes as in panels E and F. (**I**) The latency from the stimulus onset to the maximum of ACC synaptic activation for varying top-down expectation $z(0)$ under naive (blue) and chronic pain (red) condition. (**J**) Similar to panel K, except for two ACC subpopulations $E_{2\text{-}1}$ (w/ direct S1 input) and $E_{2\text{-}2}$ (w/o S1). Mean and SEM for each group are shown. 100 Monte Carlo runs were run with random initial $z(0) \in [-3.0, 3.0]$. (**K**) Maximum of middle line of ACC synaptic activation variable s from total population during the duration T_s between the stimulus onset to withdrawal, for varying top-down expectation $z(0)$ under naive (blue) and chronic pain (red) condition. (**L**) Similar to panel I, except for two ACC subpopulations $E_{2\text{-}1}$ (w/ direct S1 input) and $E_{2\text{-}2}$ (w/o S1).

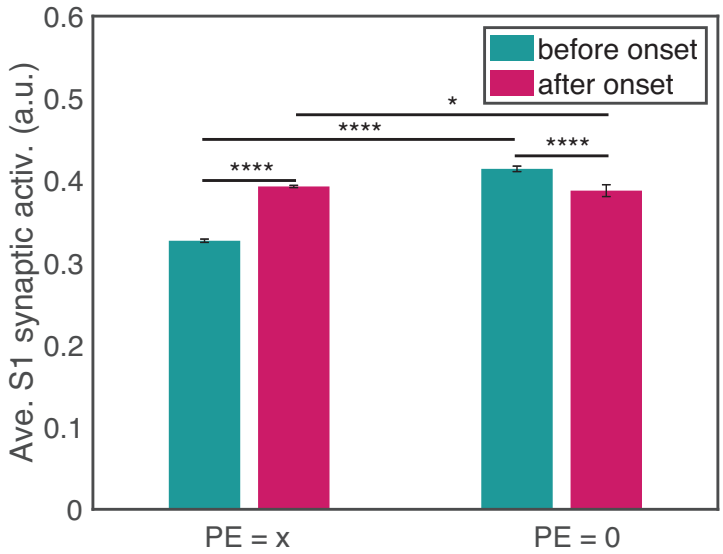

Fig S5. Comparison of average S1 synaptic activation at different periods (before vs. after onset) and PE values: PE= x (or $z = 0$) and PE= 0 (or $z = x$), with feedback from the ACC to S1. A total of 15 Monte Carlo trials were run with random $x(0) \in [1.8, 2.2]$. Mean and SEM were presented for each group. There was a significant difference in the average S1 synaptic activation variable between before and after stimulus in both conditions. All p-values for pairs marked in the graph are less than 0.0001, expect for the $p = 0.0138$ between PE= x and PE= 0 after onset (two pink bars). This indicates that the decrease in S1 firing intensity after the stimulus onset was less significant with the presence of feedback. The firing before stimulus was computed from the expectation z onset (from 0 if no expectation) to the stimulus x onset; the firing after stimulus was computed from the stimulus onset to withdrawal. Compared to Fig. 10C, the gap between before and after stimulus was smaller here.